A size-dependent meshfree model based on nonlocal strain gradient theory for trigonometric functionally graded nanoplates on variable elastic foundations

Xuebing Zhang[a], Baikuang Chen[a], Zhanjun Shao[b], A. S. Ademiloye[c], Delei Yang[d], Ping Xiang[b,e,*], Wang Xianbiao[f]

[a]*College of Civil Engineering, Xiangtan University, Xiangtan 411105, China;*
[b]*School of Civil Engineering, Central South University, Changsha 410075, China;*
[c]*Zienkiewicz Institute for Modelling, Data and AI, Faculty of Science and Engineering, Swansea University, Swansea, United Kingdom;*
[d]*College of Building Engineering, Huanghuai University, Henan Province 463000, China;*
[e]*National Engineering Research Center of High-speed Railway Construction Technology, Changsha 410018, China;*
[f]*Anhui Provincial Key Laboratory of Advanced Building Materials, Anhui Jianzhu University, Hefei, 230601, China;*

*(*corresponding author's emails: pxiang2-c@my.cityu.edu.hk)*

Abstract

In this paper, a nonlocal strain gradient meshfree model is proposed and developed to explore the bending and vibration behaviours of a novel trigonometric functionally graded nanoplates (TFGNPs). Based on the generalized layerwise higher-shear deformation theory (GL-HSDT) and the nonlocal strain gradient theory (NSGT), a weak form of governing equations for plate motion is derived, with consideration of a two-parameter variable elastic foundation. We employed a cosine function to describe the material gradation of TFGNPs along their thickness while the size-scale effect in nanoplates was effectively captured through the incorporation of NSGT. The radial point interpolation method, which possesses high continuum and Kronecker delta function properties, is employed to develop a meshfree formulation for the discrete solution of governing equations. By comparing the results of the study with those in existing literature, the correctness and high accuracy of present model is verified. It is shown that the material properties of TFGNPs possess high stability and continuous, smooth stress variations. Moreover, a comprehensive parametric study is conducted to determine the sensitivity of the bending and vibration responses of TFGNPs to boundary conditions, geometries, foundation parameters, nonlocal and strain gradient parameters.

Keyword: Trigonometric functionally graded nanoplates; Nonlocal strain gradient theory; Size-dependent meshfree model; Radial point interpolation method; Variable elastic foundation.

1. Introduction

Composite structures are increasingly utilized in civil, mechanical, aerospace, and medical engineering due to their exceptional mechanical, chemical, and electronic properties [1,2]. Numerous studies have focused on the design, fabrication, and analysis of composite materials. He et al. [3] synthesized the $LaFeO_3/Fe_3O_4/C$ perovskite composites by one-step pyrolysis of 3d-4f metal-organic frameworks (MOFs) at a low temperature. Dong et al. [4] investigated the mechanical properties of rubberized concrete enhanced by basalt fiber-epoxy resin composite based on experimental testing and numerical simulations. For sandwich composite structures, Liu et al. [5] examined the structural response of the U-type corrugated core sandwich panel used in ship structures under loading, while Cen et al. [6] optimized the molding process of foam sandwich wing structures. Further, a recognition and optimisation method of impact deformation patterns based on point cloud and deep clustering was applied to thin-walled tubes [7]. Functionally graded nanomaterials (FGMs) are a new type of non-homogeneous composites with continuous smooth variation of material properties along the thickness, which are promising for engineering applications. Many efforts have been devoted to the static, vibration and buckling analysis of FG structures, such as shells [8], plates [9], beams [10], etc. Among all, FG sandwich nanoplates have gained popularity as structural components of significant importance.

In recent decades, a variety of analytical theories for laminated composites and sandwich plates have been developed, mainly including the equivalent single-layer model and layerwise model [11,12]. Classical laminate plate theory [13] is characterized by neglecting transverse shear deformation effect and obtains poor results when employed to calculate medium and thick plates. First-order shear deformation theory [14] is applicable to both moderately thick and thin plates, but the shear correction factor causes significant effect on the accuracy of its solution. Higher-order shear deformation theory [15,16] has a transverse shear function that describes the nonlinear variation of the transverse shear stress along the plate thickness, providing more accurate results for displacement and transverse shear stress. Most of these deformation theories use the equivalent single-layer model. However, owing to the variations in material properties between different laminates, equivalent single-layer model fails to accurately represent the transverse shear stress between the layers. Therefore, layerwise theories that impose independent degrees of freedom for each layer were developed. Notably, the generalized layerwise model by Reddy [17] and the simple linear layerwise theory by Ferreiral [18] have received much attention. Several other 'r' layerwise or zigzag models have been presented by Mau [19], Di Sciuva [20] and Toledano et al. [21]. Particularly, for the nonlinear layerwise theory, Thai et al. [22] proposed a generalized layerwise higher-order shear deformation theory (GL-HSDT), which ensures continuity of the interface layer displacement field and the transverse shear stress field. Compared with other layerwise theories, Thai's theory avoids constant interlayer transverse stresses and retains a minimum number of variables. Subsequently, Phan-Dao [23] applied this theory in free vibration, static, and buckling analyses of composite sandwich plates, and the results showed that it could produce higher accuracy of interlayer shear stresses.

For micro and nanostructures, the behaviours of materials at nanoscale level are very different from those at the macroscale level. Therefore, improved continuum mechanics models are needed to account for small-scale effects. For instance, Eringen [24] proposed a nonlocal elasticity theory for nanostructures that considers higher-order derivatives of stresses. Mindlin [25] and Aifantis [26] developed a strain gradient theory by introducing higher order derivatives of strains into the elasticity theory. Additionally, various theoretical models, including modified coupled stress theory [27] and modified strain gradient theory [28,29], were employed to simulate the computation of micro and nanostructures. Phung-Van et al. investigated the nonlinear behaviour of magneto-electro-elastic porous nanoplates [30] and FG piezoelectric porous nanoplates [31] by combining nonlocal Eringen's theory and isogeometric analysis. Nguyen et al. [32] analyzed buckling, bending and free vibration behaviours of metal foam microbeams based on the modified strain gradient theory. Nevertheless, all of these theories only consider the nonlocal effects or strain gradient effects individually. In order to integrate these two effects, Lim et al. [33] proposed the nonlocal strain gradient theory (NSGT). Thai et al. established an isogeometric analysis model integrating the NSGT and NURBS basis functions, which was utilized to examined the bending [34], free vibration [35] and nonlinear dynamic behaviour [36] of nanoplates. Also, they developed a size-dependent meshfree method based on NSGT for the comparative study of mechanical behaviour of FG sandwich nanoplates [37]. Recently, Phung-Van et al. [38,39] applied NSGT to examined the small-scale effect and nonlinear effect in FG triply periodic minimal surface nanoplates. Additionally, they investigated the size-dependent behaviour of honeycomb sandwich nanoplates [40] and FG graphene platelet-reinforced composites plates [41]. Based on NSGT, Nguyen-Xuan et al. [42,43] analysed the effects of parameters such as power index, geometrical parameters, nonlocal and strain gradients on the magneto-electro-elastic FG nanoplates. Elastic foundations have a wide range of engineering applications including road bridges, skyscrapers and pipeline networks [44,45]. Daikh et al. [46] analysed the static bending of FG beams and plates on the Winkler elastic foundation using a quasi-3D shear deformation theory. Sobhy [47] studied the bending, buckling and vibration response of FG nonlocal sandwiched nanoplates subject to Winkler's two-parameter elastomeric foundations, which utilized the finite element method.

It can be observed that the primary approaches for solving nonlocal strain gradient nanostructures include analytical and numerical methods. Analytical solution provides accurate results, but it is confined to simple problems. In contrast to finite element method and isogeometric analysis method, meshfree methods have no mesh constraints and enable a computation of displacement and stress at arbitrary points in physical space [48,49]. Moreover, the approximation function of meshfree method is commonly high-order continuous, which satisfies the higher-order derivative requirement of NSGT. In recent years, meshfree method has been successfully applied to a variety of engineering problems, examples of which include deformation of nanomaterials [50], static and vibration analysis of nano beams/plates/shells [51–53], biomechanical problems [54,55], etc. Particularly, the radial point interpolation method (RPIM) may be convenient as its Kronecker delta function property, which permits the imposition of essential boundary conditions in the same way as in conventional finite element method.

A review of the above literature shows that researches on composite sandwich nanoplates mainly focus on how to develop a suitable theoretical model to analyse their mechanical properties. These explorations involve the application of laminate theory, the consideration of size-scale effects and the selection of numerical methods. However, another often overlooked issue is that in conventional FG sandwich nanoplates, the significant divergence in stiffness between ceramics and metals leads to abrupt alterations in physical characteristics (e.g., stress-strain) at the interface of the core and surface layers, which may trigger interfacial debonding. Addressing this, the research innovatively proposes a novel trigonometric functionally graded nanoplates (TFGNPs). This design achieves a perfect mixture of ceramics and metals as well as a smooth and continuous material transitions, effectively mitigating the problem of stress discontinuities. Furthermore, we combined the GL-HSDT, NSGT and RPIM meshfree method for the first time to develop a size-dependent model that takes into account the effects of the variable elasticity foundations. The model describes the nonlocal effect and strain gradient effect of nanoscale plates by using two relevant scale parameters. While the model reverts to a classical elasticity theory model when both two scale parameters are set to zero. Thus, the developed model provides a high precision tool for a comprehensive observation of the complex mechanical behaviours of nanoplates from the macroscopic to microscopic level. In this paper, the effects of boundary conditions, geometry, foundation parameters, nonlocal and strain gradient parameters on TFGNPs are discussed in detail. Numerical results not only verify the correctness of the model, but also demonstrate the potential of novel TFGNPs for engineering applications, highlighting the dual innovation of this research.

2. Theoretical model

2.1 Functionally graded nanoplates

Consider rectangular functionally graded nanoplates of thickness h, length a and width b, which are located on the elastic foundation, as shown in Fig. 1. The origin of coordinate system is situated at the corner point of the midplane, and the edges of plates are parallel to the x-axes and y-axes. Fig. 1(a) is conventional functionally graded sandwich nanoplates (FGSNPs), which consists of two functionally graded surface layers and a ceramic core layer. Fig. 1(b) are TFGNPs proposed in this study, including the trigonometric functionally graded nanoplate of type A "TFGNP-A" and the trigonometric functionally graded nanoplate of type B "TFGNP-B". The ceramic volume rate of each layer of TFGNPs is represented by a unified cosine function, whereas TFGNP-A and TFGNP-B are distinguished by their use of different cosine functions. The vertical coordinates of plates' bottom, two interfaces, and top are denoted by h_0, h_1, h_2, h_3. In this paper, unless specified, all the functionally graded plates use a 1-1-1 sandwich configuration, that is, the top, core and bottom layers of plates are of equal thickness.

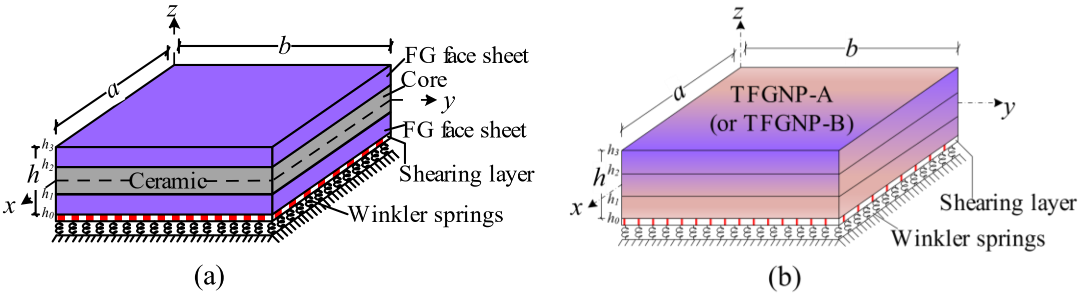

Fig. 1 The geometric configuration of functionally graded plates: (a) FGSNPs; (b) TFGNPs.

For the FGSNPs, the ceramic volume rate of each layer $V^{(k)}(z)$ is expressed by different power-law functions as [56],

$$V^{(1)}(z)=\left(\frac{z-h_0}{h_1-h_0}\right)^p,\quad h_0\le z\le h_1;$$
$$V^{(2)}(z)=1,\quad h_1\le z\le h_2;$$
$$V^{(3)}(z)=\left(\frac{z-h_3}{h_2-h_3}\right)^p,\quad h_2\le z\le h_3. \tag{1}$$

For the TFGNP-A, the ceramic volume rate of each layer $V^{(k)}(z)$ is expressed by the unified cosine function as,

$$V^{(k)}(z)=\frac{1}{2}\left(1+\cos\left(N\frac{2\pi z}{h}\right)\right),\quad N=1,\ 3,\ 5\ \ldots$$
$$V^{(k)}(z)=\frac{1}{2}\left(1-\cos\left(N\frac{2\pi z}{h}\right)\right),\quad N=2,\ 4,\ 6\ \ldots \tag{2}$$

For the TFGNP-B, the ceramic volume rate of each layer $V^{(k)}(z)$ is represented by the unified cosine function as,

$$V^{(k)}(z)=\frac{1}{2}\left(1+\cos\left(N\frac{2\pi z}{h}\right)\right),\quad N=2,\ 4,\ 6\ \ldots$$
$$V^{(k)}(z)=\frac{1}{2}\left(1-\cos\left(N\frac{2\pi z}{h}\right)\right),\quad N=1,\ 3,\ 5\ \ldots \tag{3}$$

The variation of volume rate for ceramics along the thickness distribution is plotted in Figs. 2 and 3 for FGSNPs, TFGNP-A and TFGNP-B, respectively.

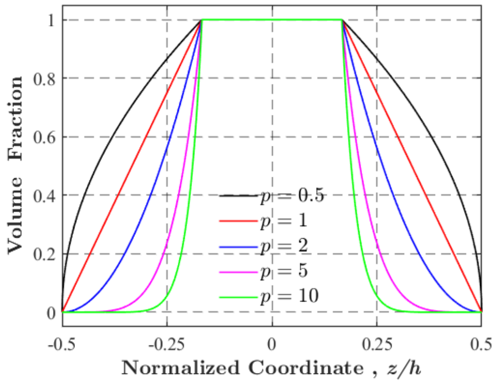

Fig. 2 The variation of the volume fraction for ceramics along the thickness of FGSNPs with different power-law exponent p.

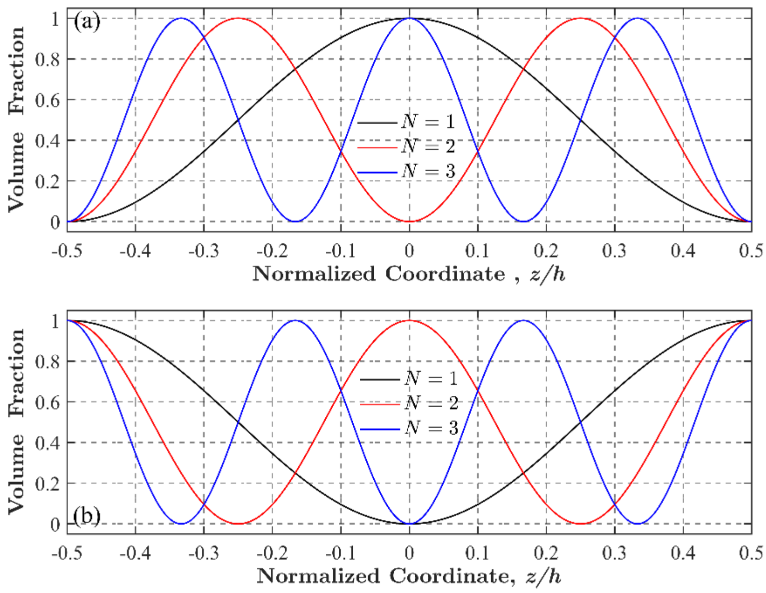

Fig. 3 The variation of the volume fraction for ceramics along the thickness of TFGNPs with different parameter N: (a)TFGNP-A; (b)TFGNP-B.

For a better representation of the differences between the proposed TFGNPs and the conventional FGSNPs, Fig. 4 displays the percentage (%) of ceramic composition in TFGNPs as well as FGSNPs with various sandwich structures. Here, the total ceramic content in FGSNPs varies with the power-law exponent p and sandwich configuration. Nevertheless, the TFGNPs have 50% ceramics while the remaining 50% is metal, regardless of the parameter N and sandwich configuration. Moreover, for the TFGNP-A and TFGNP-B, the percentage of ceramic constituent in each layer is shown in Fig. 5. Although the total percentage of ceramic components in TFGNPs remains constant, the ceramic content of each layer changes as N varies.

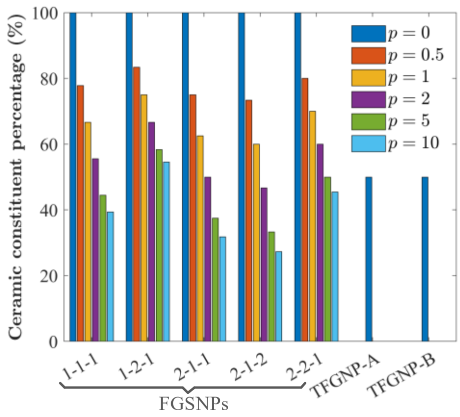

Fig. 4 Percentage of total ceramic constituent in TFGNP-A, TFGNP-B and FGSNPs with different sandwich configurations.

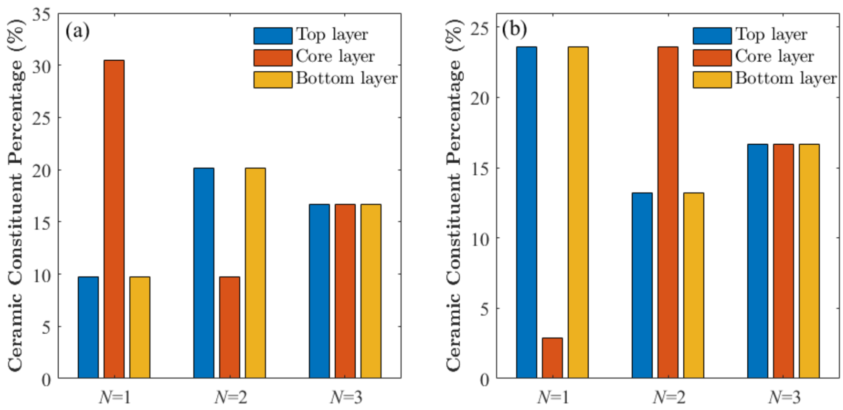

Fig. 5 Percentage of ceramic constituent in each layer of TFGNPs: (a)TFGNP-A; (b)TFGNP-B.

According to a mixture rule [46], the effective material properties of the *k*-th layer can be calculated as,

$$P^{(k)}(z) = P_{\mathrm{m}} + \left(P_{\mathrm{c}} - P_{\mathrm{m}}\right)V^{(k)}(z) \tag{4}$$

where P represents the effective material properties such as Young's modulus E, density ρ and Poisson's ratio v. The subscripts ‘m’ and ‘c’ denote the metal and ceramic compositions, respectively.

2.2 Nonlocal strain gradient theory

Taking into account the effects of both the nonlocal stress field and the strain gradient stress field, the general nonlocal stress tensor can be expressed as [37],

$$t_{ij} = t_{ij}^{(0)} - \nabla t_{ij}^{(1)} \tag{5}$$

in which

$$t_{ij}^{(0)}(\mathbf{x}) = \int_V \alpha\left(|\mathbf{x}'-\mathbf{x}|\right)\sigma_{ij}\left(\mathbf{x}'\right)\mathrm{d}V'\left(\mathbf{x}'\right),$$

$$t_{ij}^{(1)}(\mathbf{x}) = l^2\int_V \alpha\left(|\mathbf{x}'-\mathbf{x}|\right)\nabla\sigma_{ij}\left(\mathbf{x}'\right)\mathrm{d}V'\left(\mathbf{x}'\right) \tag{6}$$

where $t_{ij}^{(0)}$ and $t_{ij}^{(1)}$ are linear and higher-order nonlocal stress tensors, respectively; $\mathbf{x}$ is arbitrary point in V; $\alpha(|\mathbf{x}'-\mathbf{x}|)$ is a nonlocal kernel function; l is the material length dimension parameter; and σ_{ij} is a local stress tensor satisfying the following conditions,

$$\sigma_{ij} = C_{ijkl}\varepsilon_{kl},\quad \varepsilon_{kl} = \frac{1}{2}\left(u_{k,l} + u_{l,k}\right) \tag{7}$$

where C_{ijkl} is the modulus of elasticity coefficient; ε_{kl} and u_k are the strain and displacement components, respectively.

Using a special Helmholtz averaging kernel [34], the nonlocal instanton relation in Eq. (6) can be rewritten as,

$$Lt_{ij}^{(0)} = \sigma_{ij},\ Lt_{ij}^{(0)} = \lambda\nabla\sigma_{ij},\ Lt_{ij,j}^{(0)} = \sigma_{ij,j},\ Lt_{ij,j}^{(1)} = \lambda\nabla\sigma_{ij,j} \tag{8}$$

where $L = (1-\mu\nabla^2)$ is a linear differential operator, $\nabla^2 = \partial^2/\partial x^2 + \partial^2/\partial y^2$ is a Laplace operator; $\lambda = l^2$ is a strain gradient parameter used to represent the effect of the strain gradient field; and μ is a nonlocal parameter determined by the lattice spacing between individual atoms and the grain size, which describes the interactions between particles within the material.

Similarly, Eq. (5) can be rewritten as,

$$Lt_{ij} = Lt_{ij}^{(0)} - L\nabla t_{ij}^{(1)},\ Lt_{ij,j} = Lt_{ij,j}^{(0)} - L\nabla t_{ij,j}^{(1)} \tag{9}$$

The equation of motion for nonlocal linear elastic solids is expressed as [57],

$$t_{ij,j} + f_i = \rho\ddot{u}_i \ \text{ in } \ V \tag{10}$$

$$n_i t_{ij} = g_i \ \text{ on } \Gamma \tag{11}$$

where t_{ij}, f_i, $g_i, \ddot{u}_i, \rho, n_i, V$ and $\Gamma$are the general nonlocal stress vector, force vector, traction vector, acceleration vector, mass density, normal vector, volume and boundary, respectively.

According to Eq. (10), the expression for the balance equation can be obtained by substituting Eq. (8) into Eq. (9),

$$\sigma_{ij,j} - \lambda\nabla^2\sigma_{ij,j} + (1-\mu\nabla^2)f_i = (1-\mu\nabla^2)\rho\ddot{u}_i \tag{12}$$

Applying the principle of virtual work, the integral form of the balance equation is expressed as,

$$\int_V \sigma_{ij,j}\delta u_i \mathrm{d}V - \lambda\int_V \nabla^2\sigma_{ij,j}\delta u_i\mathrm{d}V + \int_V\left(1-\mu\nabla^2\right)f_i\delta u_i\mathrm{d}V = \int_V\left(1-\mu\nabla^2\right)\rho\ddot{u}_i\delta u_i\mathrm{d}V \tag{13}$$

in which δu_i is the virtual displacement.

Applying the partial integral and the scattering theorem to the first and second parts of Eq. (13), respectively, yields,

$$\int_V \sigma_{ij,j}\delta u_i \mathrm{d}V = -\int_V \sigma_{ij}\delta u_{i,j}\mathrm{d}V + \int_{\Gamma_g} \sigma_{ij}n_i\delta u_i \mathrm{d}\Gamma_g \tag{14}$$

$$\int_V \nabla^2\sigma_{ij,j}\delta u_i \mathrm{d}V = -\int_V \sigma_{ij}\delta u_{i,j}\mathrm{d}V + \int_{\Gamma_g} \nabla^2\sigma_{ij}n_i\delta u_i \mathrm{d}\Gamma_g \tag{15}$$

in which Γ_g is Neumann boundary condition.

Substituting Eqs. (14) and (15) into Eq. (13), the final integral form of the balance equation is described as,

$$\begin{aligned} &-\int_V \sigma_{ij}\delta u_{i,j}\mathrm{d}V + \int_{\Gamma_g} \sigma_{ij}n_i\delta u_i \mathrm{d}\Gamma_g + \lambda\int_V \sigma_{ij}\delta u_{i,j}\mathrm{d}V - \lambda\int_{\Gamma_g} \nabla^2\sigma_{ij}n_i\delta u_i \mathrm{d}\Gamma_g \\ &+\int_V \left(1-\mu\nabla^2\right) f_i\delta u_i \mathrm{d}V = \int_V \left(1-\mu\nabla^2\right)\rho\ddot{u}_i\delta u_i \mathrm{d}V \end{aligned} \tag{16}$$

By imposing symmetry conditions, the virtual displacement vector can be written as,

$$\delta u_{i,j} = \frac{1}{2}\left(\delta u_{i,j} + \delta u_{j,i}\right) \tag{17}$$

In this study, the traction on the Neumann boundary is neglected [34]. Substituting Eq. (17) into Eq. (16), the final integral form of the balance equation is formulated as,

$$\int_V \sigma_{ij}\delta\varepsilon_{ij}\mathrm{d}V - \lambda\int_V \nabla^2\sigma_{ij}\delta\varepsilon_{ij}\mathrm{d}V + \int_V \left(1-\mu\nabla^2\right)\rho\ddot{u}_i\delta u_i \mathrm{d}V = \int_V \left(1-\mu\nabla^2\right) f_i\delta u_i \mathrm{d}V \tag{18}$$

2.3 A generalized layerwise higher-shear deformation theory

2.3.1 Displacements, strains and stress in the plates

For a multi-layer laminate structure as shown in Fig.1, according to the generalized layerwise higher order shear deformation theory presented by Thai et al. [22], the displacement field at arbitrary point of the k-th layer can be expressed as,

$$\begin{aligned} u^{(k)}(x,y,z) &= u_0(x,y) - z\frac{\partial w_0(x,y)}{\partial x} + \left[A^{(k)} + zB^{(k)} + f(z)\right]\phi_x(x,y), \\ v^{(k)}(x,y,z) &= v_0(x,y) - z\frac{\partial w_0(x,y)}{\partial y} + \left[C^{(k)} + zD^{(k)} + f(z)\right]\phi_y(x,y), \\ w^{(k)}(x,y,z) &= w_0(x,y) \end{aligned} \tag{19}$$

where $u^{(k)}$ and $v^{(k)}$ are the in-plane displacements at any point (x, y, z) of the k-th layer; u_0, v_0 and w_0 are the displacement components of the mid-plane along the x, y, z directions; ϕ_x and ϕ_y are the rotational inertia of the mid-plane about y-axis and x-axis, respectively.

Imposing continuity conditions within the interfacial surfaces of the layers yields the parameters $A^{(k)}$ and $C^{(k)}$,

$$\begin{cases} u^{(k-1)}(x,y,z) = u^{(k)}(x,y,z) \\ v^{(k-1)}(x,y,z) = v^{(k)}(x,y,z) \end{cases} \Rightarrow \begin{cases} A^{(k)} = A^{(k-1)} + z^{(k)}(B^{(k-1)} - B^{(k)}) \\ C^{(k)} = C^{(k-1)} + z^{(k)}(D^{(k-1)} - D^{(k)}) \end{cases} \tag{20}$$

in which the parameters $B^{(k)}$ and $D^{(k)}$ are determined later.

The displacement field of Eq. (19) can be written in compact form as follows,

$$\boldsymbol{u}^{(k)} = \boldsymbol{u}_0 + z\boldsymbol{u}_1 + f(z)\boldsymbol{u}_2 \tag{21}$$

with

$$\boldsymbol{u}_0 = \begin{Bmatrix} u_0 + A^{(k)}\phi_x \\ v_0 + C^{(k)}\phi_y \\ w_0 \end{Bmatrix};\ \boldsymbol{u}_1 = \begin{Bmatrix} -w_{0,x} + B^{(k)}\phi_x \\ -w_{0,y} + D^{(k)}\phi_y \\ 0 \end{Bmatrix};\ \boldsymbol{u}_2 \begin{Bmatrix} \phi_x \\ \phi_y \\ 0 \end{Bmatrix} \tag{22}$$

In classical lamination theory, the shear stress does not satisfy the condition of vanishing on the upper and lower surfaces of the plate, so a nonlinear displacement term is introduced in Eq. (19) to solve this problem by a shape function $f(z)$ in the thickness direction of the laminate. In this study, $f(z) = z - 4z^3/(3h^2)$ proposed by Reddy [58] is adopted.

The displacement-strain relations for layer k can be written as,

$$\begin{aligned} \boldsymbol{\varepsilon}^{(k)} &= \begin{Bmatrix} \varepsilon_{xx} & \varepsilon_{yy} & \tau_{xy} \end{Bmatrix}^{\mathrm{T}} = \boldsymbol{\varepsilon}_0 + z\boldsymbol{\varepsilon}_1 + f(z)\boldsymbol{\varepsilon}_2, \\ \boldsymbol{\tau}^{(k)} &= \begin{Bmatrix} \tau_{xz} & \tau_{yz} \end{Bmatrix}^{\mathrm{T}} = \boldsymbol{\varepsilon}_0^{\mathrm{s}} + f'(z)\boldsymbol{\varepsilon}_1^{\mathrm{s}} \end{aligned} \tag{23}$$

with

$$\boldsymbol{\varepsilon}_0 = \begin{Bmatrix} u_{0,x} + A^{(k)}\phi_{x,x} \\ v_{0,x} + C^{(k)}\phi_{y,y} \\ u_{0,y} + v_{0,x} + A^{(k)}\phi_{x,y} + C^{(k)}\phi_{y,x} \end{Bmatrix},\ \boldsymbol{\varepsilon}_1 = \begin{Bmatrix} -w_{0,xx} + B^{(k)}\phi_{x,x} \\ -w_{0,yy} + D^{(k)}\phi_{y,y} \\ -2w_{0,xy} + B^{(k)}\phi_{x,y} + D^{(k)}\phi_{y,x} \end{Bmatrix},$$

$$\boldsymbol{\varepsilon}_2 = \begin{Bmatrix} \phi_{x,x} \\ \phi_{y,y} \\ 2\phi_{x,y} \end{Bmatrix},\ \boldsymbol{\varepsilon}_0^{\mathrm{s}} = \begin{Bmatrix} B^{(k)}\phi_x \\ D^{(k)}\phi_y \end{Bmatrix},\ \boldsymbol{\varepsilon}_1^{\mathrm{s}} = \begin{Bmatrix} \phi_x \\ \phi_y \end{Bmatrix}. \tag{24}$$

By neglecting $\sigma_z^{(k)} = \sigma_3^{(k)}$ for each orthogonal layer in the laminate structure, the constitutive equation for the k-th orthogonal layer of laminate can be expressed as,

$$\begin{Bmatrix} \sigma_{xx}^{(k)} \\ \sigma_{yy}^{(k)} \\ \tau_{xy}^{(k)} \\ \tau_{xz}^{(k)} \\ \tau_{yz}^{(k)} \end{Bmatrix} = \begin{bmatrix} Q_{11}^{(k)} & Q_{12}^{(k)} & 0 & 0 & 0 \\ Q_{12}^{(k)} & Q_{22}^{(k)} & 0 & 0 & 0 \\ 0 & 0 & Q_{66}^{(k)} & 0 & 0 \\ 0 & 0 & 0 & Q_{55}^{(k)} & 0 \\ 0 & 0 & 0 & 0 & Q_{44}^{(k)} \end{bmatrix} \begin{Bmatrix} \varepsilon_{xx}^{(k)} \\ \varepsilon_{yy}^{(k)} \\ \gamma_{xy}^{(k)} \\ \gamma_{xz}^{(k)} \\ \gamma_{yz}^{(k)} \end{Bmatrix} \tag{25}$$

where $Q_{ij}^{(k)}$ is calculated as follows,

$$Q_{11}^{(k)} = \frac{E_1^{(k)}(z)}{1-\nu_{12}^{(k)}\nu_{21}^{(k)}},\ Q_{12}^{(k)} = \frac{\nu_{12}^{(k)}E_2^{(k)}(z)}{1-\nu_{12}^{(k)}\nu_{21}^{(k)}},\ Q_{22} = \frac{E_2^{(k)}(z)}{1-\nu_{12}^{(k)}\nu_{21}^{(k)}},$$
$$Q_{66}^{(k)} = G_{12}^{(k)},\ Q_{44}^{(k)} = G_{23}^{(k)},\ Q_{55}^{(k)} = G_{13}^{(k)},\ \nu_{12}^{(k)} = \nu_{21}^{(k)}E_2^{(k)}(z)/E_1^{(k)}(z) \tag{26}$$

in which $E_1^{(k)}(z)$ and $E_2^{(k)}(z)$ are Young's moduli varying along the thickness, $G_{12}^{(k)}$, $G_{23}^{(k)}$ and $G_{13}^{(k)}$ are shear moduli; $\nu_{12}^{(k)}$ and $\nu_{21}^{(k)}$ are Poisson's ratios. Subscripts 1, 2 and 3 correspond to the x, y and z directions. The FG nanoplates in this study consist of isotropic elastic layers that can be written as,

$$Q_{11}^{(k)} = Q_{22}^{(k)} = \frac{E^{(k)}(z)}{1-\nu^2},\ Q_{12}^{(k)} = Q_{21}^{(k)} = \frac{\nu E^{(k)}(z)}{1-\nu^2},$$
$$Q_{66}^{(k)} = Q_{55}^{(k)} = Q_{44}^{(k)} = \frac{E^{(k)}(z)}{2(1+\nu)} \tag{27}$$

According to Eqs. (19) and (25), the transverse shear stress in each layer can be rewritten as,

$$\begin{cases} \tau_{xz}^{(k)} = Q_{55}^{(k)}\gamma_{xz}^{(k)} = Q_{55}^{(k)}\left(B^{(k)}\phi_x + f'(z)\phi_x\right) \\ \tau_{yz}^{(k)} = Q_{44}^{(k)}\gamma_{yz}^{(k)} = Q_{44}^{(k)}\left(D^{(k)}\phi_y + f'(z)\phi_y\right) \end{cases} \tag{28}$$

Applying the continuity condition to the transverse shear stresses at the interfaces of layers yields,

$$\begin{matrix} \tau_{xz}^{(k-1)} = \tau_{xz}^{(k)} \\ \tau_{yz}^{(k-1)} = \tau_{yz}^{(k)} \end{matrix} \Rightarrow \begin{cases} Q_{55}^{(k-1)}\left(B^{(k-1)}\phi_x + f'(z)\phi_x\right) = Q_{55}^{(k)}\left(B^{(k)}\phi_x + f'(z)\phi_x\right) \\ Q_{44}^{(k-1)}\left(D^{(k-1)}\phi_y + f'(z)\phi_y\right) = Q_{44}^{(k)}\left(D^{(k)}\phi_y + f'(z)\phi_y\right) \end{cases} \tag{29}$$

Eq. (29) can be rewritten as,

$$B^{(k)} = \frac{Q_{55}^{(k-1)}}{Q_{55}^{(k)}}B^{(k-1)} + f'(z)\left(\frac{Q_{55}^{(k-1)}}{Q_{55}^{(k)}} - 1\right)$$
$$D^{(k)} = \frac{Q_{44}^{(k-1)}}{Q_{44}^{(k)}}D^{(k-1)} + f'(z)\left(\frac{Q_{44}^{(k-1)}}{Q_{44}^{(k)}} - 1\right) \tag{30}$$

Note that the parameters for the first layer of symmetric laminates are defined by,

$$B^{(1)} = 0,\ A^{(1)} = -\sum_{i=2}^{k_{\text{midplane}}} z(i)\left(B^{(i-1)} - B^{(i)}\right)$$
$$D^{(1)} = 0,\ \mathrm{C}^{(1)} = -\sum_{i=2}^{k_{\text{midplane}}} z(i)\left(D^{(i-1)} - D^{(i)}\right) \tag{31}$$

2.3.2 Weak form of the governing equation

Considering Winkler elastic foundation and uniform sinusoidal transverse loads, the governing equations for static bending of the k-th layer plate are obtained by substituting Eqs. (23) - (25) into Eq. (18) as follows,

$$
\begin{aligned}
&\int_\Omega \delta\bar{\boldsymbol{\varepsilon}}^{\mathrm{T}}\boldsymbol{Q}_{\mathrm{b}}^{(k)}\bar{\boldsymbol{\varepsilon}}\mathrm{d}\Omega-\lambda\int_\Omega \delta\left(\nabla^2\bar{\boldsymbol{\varepsilon}}^{\mathrm{T}}\right)\boldsymbol{Q}_{\mathrm{b}}^{(k)}\bar{\boldsymbol{\varepsilon}}\mathrm{d}\Omega+\int_\Omega \delta\bar{\boldsymbol{\gamma}}^{\mathrm{T}}\boldsymbol{Q}_{\mathrm{s}}^{(k)}\bar{\boldsymbol{\gamma}}\mathrm{d}\Omega-\lambda\int_\Omega \delta\left(\nabla^2\bar{\boldsymbol{\gamma}}^{\mathrm{T}}\right)\boldsymbol{Q}_{\mathrm{s}}^{(k)}\bar{\boldsymbol{\gamma}}\mathrm{d}\Omega\\
&+\int_\Omega\left(1-\mu\nabla^2\right)\delta w k_{\mathrm{w}}\,w\mathrm{d}\Omega=\int_\Omega\left(1-\mu\nabla^2\right)\delta w q_0\mathrm{d}\Omega
\end{aligned}
\tag{32}
$$

with

$$
\bar{\boldsymbol{\varepsilon}}=\begin{Bmatrix}\boldsymbol{\varepsilon}_0\\ \boldsymbol{\varepsilon}_1\\ \boldsymbol{\varepsilon}_2\end{Bmatrix},\ \bar{\boldsymbol{\gamma}}=\begin{Bmatrix}\boldsymbol{\varepsilon}_0^{\mathrm{s}}\\ \boldsymbol{\varepsilon}_1^{\mathrm{s}}\end{Bmatrix},\ \boldsymbol{Q}_{\mathrm{b}}^{(k)}=\begin{bmatrix}\mathbf{A}&\mathbf{B}&\mathbf{E}\\ \mathbf{B}&\mathbf{D}&\mathbf{F}\\ \mathbf{E}&\mathbf{F}&\mathbf{H}\end{bmatrix}^{(k)},\ \boldsymbol{Q}_{\mathrm{s}}^{(k)}=\begin{bmatrix}\mathbf{A}^{\mathrm{s}}&\mathbf{B}^{\mathrm{s}}\\ \mathbf{B}^{\mathrm{s}}&\mathbf{D}^{\mathrm{s}}\end{bmatrix}^{(k)},
$$

$$
\begin{aligned}
&\left(A_{ij},B_{ij},D_{ij},E_{ij},F_{ij},H_{ij}\right)^{(k)}=\int_{-h^{(k)}/2}^{h^{(k)}/2}\left(1,z.z^2,f(z),zf(z),f^2(z)\right)Q_{ij}^{(k)}\mathrm{d}z\quad \text{where } (i,\ j=1,\ 2,\ 6),\\
&(A_{ij}^{\mathrm{s}},\ B_{ij}^{\mathrm{s}},\ D_{ij}^{\mathrm{s}})^{(k)}=\int_{-h^{(k)}/2}^{h^{(k)}/2}\left(1,\ f'(z),\ f'^2(z)\right)Q_{ij}^{(k)}\ \mathrm{d}z\ \ \text{where } (i,\ j=4,\ 5).
\end{aligned}
\tag{33}
$$

Similarly, the governing equation for free vibration can be expressed as,

$$
\begin{aligned}
&\int_\Omega \delta\bar{\boldsymbol{\varepsilon}}^{\mathrm{T}}\boldsymbol{Q}_{\mathrm{b}}^{(k)}\bar{\boldsymbol{\varepsilon}}\mathrm{d}\Omega-\lambda\int_\Omega \delta\left(\nabla^2\bar{\boldsymbol{\varepsilon}}^{\mathrm{T}}\right)\boldsymbol{Q}_{\mathrm{b}}^{(k)}\bar{\boldsymbol{\varepsilon}}\mathrm{d}\Omega+\int_\Omega \delta\bar{\boldsymbol{\gamma}}^{\mathrm{T}}\boldsymbol{Q}_{\mathrm{s}}^{(k)}\bar{\boldsymbol{\gamma}}\mathrm{d}\Omega-\lambda\int_\Omega \delta\left(\nabla^2\bar{\boldsymbol{\gamma}}^{\mathrm{T}}\right)\boldsymbol{Q}_{\mathrm{s}}^{(k)}\bar{\boldsymbol{\gamma}}\mathrm{d}\Omega\\
&+\int_\Omega\left(1-\mu\nabla^2\right)\delta w k_{\mathrm{w}}\,w\mathrm{d}\Omega+\int_\Omega\left(1-\mu\nabla^2\right)\delta\bar{\boldsymbol{u}}^{\mathrm{T}}\boldsymbol{I}_{\mathrm{m}}^{(k)}\ddot{\bar{\boldsymbol{u}}}\mathrm{d}\Omega=0
\end{aligned}
\tag{34}
$$

with

$$
\bar{\boldsymbol{u}}=\begin{Bmatrix}\boldsymbol{u}_0\\ \boldsymbol{u}_1\\ \boldsymbol{u}_2\end{Bmatrix},\ \boldsymbol{I}_{\mathrm{m}}^{(k)}=\begin{bmatrix}\boldsymbol{I}_0&\boldsymbol{I}_1&\boldsymbol{I}_3\\ \boldsymbol{I}_1&\boldsymbol{I}_2&\boldsymbol{I}_4\\ \boldsymbol{I}_3&\boldsymbol{I}_4&\boldsymbol{I}_5\end{bmatrix}^{(k)},
$$

$$
\left(\boldsymbol{I}_0,\boldsymbol{I}_1,\boldsymbol{I}_2,\boldsymbol{I}_3,\boldsymbol{I}_4,\boldsymbol{I}_5\right)^{(k)}=\int_{-h^{(k)}/2}^{h^{(k)}/2}\rho^{(k)}\left(1,z.z^2,f(z),zf(z),f^2(z)\right)\mathbf{I}_{3\times3}\mathrm{d}z \tag{35}
$$

in which $\mathbf{I}_{3\times3}$ is 3×3 unit matrix.

In Eqs. (32) and (34), k_{w} is Winkler foundation stiffness coefficient. In this paper, ignoring the effect of shear layer, two parameters κ and ξ are considered for Winkler foundations as follows,

$$k_{\mathrm{w}}=\begin{cases}\kappa+\xi\sin\left(\pi x/(2a)\right), & \text{Sinusoidal}\\ \kappa+\xi\left(1-\sin\left(\pi x/(2a)\right)\right), & \text{Reverse Sinusoidal}\\ \kappa+\xi\left(x/a\right)^{2}, & \text{Parabolic}\\ \kappa+\xi\left(1-\left(x/a\right)^{2}\right), & \text{Reverse Parabolic}\\ \kappa+\xi\left(x/a\right), & \text{Linear}\end{cases} \tag{36}$$

Additionally, the dimensionless foundation parameter is defined as,

$$K_{\mathrm{w}}=\frac{a^{4}}{D}k_{\mathrm{w}} \tag{37}$$

in which $D=\frac{h^3E_{\mathrm{c}}}{12(1-\nu^2)}$.

3. Numerical solution of RPIM

3.1 RPIM shape function

Let us consider a support domain Ω_s that has a set of arbitrarily distributed nodes as shown in Fig 6. The approximation function $u^h(\boldsymbol{x})$ can be estimated for all node values within the support domain based on radial point interpolation method (RPIM) by using radial basis function $R_i(\boldsymbol{x})$ and polynomial basis function $p_j(\boldsymbol{x})$ [59]. Nodal value of approximate function evaluated at the node $\boldsymbol{x}_i$ inside support domain is assumed to be u_i.

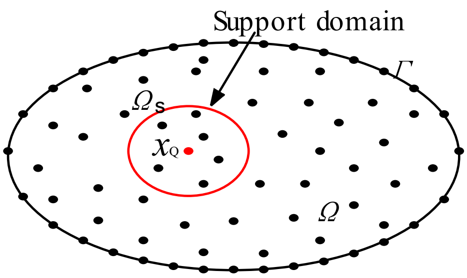

Fig. 6 Supporting domain and supporting nodes of the meshfree method.

$$u^{\mathrm{h}}(\boldsymbol{x})=\sum_{i=1}^{n}R_i(x)a_i+\sum_{j=1}^{m}p_j(x)b_j=\boldsymbol{R}^{\mathrm{T}}(\boldsymbol{x})\boldsymbol{a}+\boldsymbol{p}^{\mathrm{T}}(\boldsymbol{x})\boldsymbol{b} \tag{38}$$

where $\boldsymbol{p}(\boldsymbol{x})$ is a polynomial basis function that can be written as,

$$\boldsymbol{p}(\boldsymbol{x})=\left[p_1(x),p_2(x),\cdots,p_m(x)\right]^{\mathrm{T}} \tag{39}$$

For the two-dimensional problem, the second-order polynomial basis functions are taken as,

$$\boldsymbol{p}(\boldsymbol{x}) = \begin{bmatrix} 1 & x & y & x^2 & xy & y^2 \end{bmatrix}^{\mathrm{T}} \tag{40}$$

therefore, we have $m = 6$. And the radial basis functions $\boldsymbol{R}(\boldsymbol{x})$ is defined as,

$$\boldsymbol{R}(\boldsymbol{x}) = \left[R_1(x), R_2(x), \cdots, R_{\mathrm{n}}(x)\right]^{\mathrm{T}} \tag{41}$$

where the number of terms n is the number of support nodes in supporting domain Ω_s.

There are various commonly used radial basis functions (RBF), in this paper Multi-quadratic (MQ) radial basis function is adopted and its expression is as follows,

$$R_i(x) = \left[r^2 + (\alpha h)^2\right]^{\beta} \tag{42}$$

where r denotes the distance function, and for a two-dimension problem we have $r = \sqrt{(x - x_i)^2 + (y - y_i)^2}$; h is the average node spacing; α and β are the shape coefficients, and they are set to 1 and 1.03 respectively according to [60].

The following generic function is constructed from the set of dispersed nodes $\{x_i\}_{i=1}^{n} (\forall x_i \in \Omega_{\mathrm{s}})$ on the local support domain Ω_{s} at the computation point $\boldsymbol{x}$,

$$J_1 = \sum_{i=1}^{n} \left[\boldsymbol{R}^{\mathrm{T}}(\boldsymbol{x}_i)\boldsymbol{a} + \boldsymbol{p}^{\mathrm{T}}(\boldsymbol{x}_i)\boldsymbol{b} - \hat{u}_i\right] \tag{43}$$

$$J_2 = \sum_{i=1}^{n} p_j(x_i) b_i, \quad j = 1, 2, \cdots, m \tag{44}$$

Let $J_1 = 0$, $J_2 = 0$, Eq. (43) can be changed to the following matrix form:

$$\begin{bmatrix} \boldsymbol{R}_n & \boldsymbol{P}_m \\ \boldsymbol{P}_m^{\mathrm{T}} & \boldsymbol{0} \end{bmatrix} \begin{bmatrix} \boldsymbol{a} \\ \boldsymbol{b} \end{bmatrix} = \begin{bmatrix} \hat{\boldsymbol{U}}_s \\ \boldsymbol{0} \end{bmatrix} \tag{45}$$

where $\widehat{\boldsymbol{U}}_s$ is the vector of all the support node displacements; $\boldsymbol{R}_n$ and $\boldsymbol{P}_m$ are express as:

$$\boldsymbol{R}_n = \begin{bmatrix} R_1(x_1) & R_2(x_1) & \cdots & R_n(x_1) \\ R_1(x_2) & R_2(x_2) & \cdots & R_n(x_2) \\ \vdots & \vdots & \ddots & \vdots \\ R_1(x_n) & R_2(x_n) & \cdots & R_n(x_n) \end{bmatrix} \tag{46}$$

$$\boldsymbol{P}_m = \begin{bmatrix} p_1(x_1) & p_2(x_1) & \cdots & p_m(x_1) \\ p_1(x_2) & p_2(x_2) & \cdots & p_m(x_2) \\ \vdots & \vdots & \ddots & \vdots \\ p_1(x_n) & p_2(x_n) & \cdots & p_m(x_n) \end{bmatrix} \tag{47}$$

Solving equation (45) yields,

$$\boldsymbol{a}=\left[\boldsymbol{R}_{\boldsymbol{n}}^{-1}-\boldsymbol{R}_{\boldsymbol{n}}^{-1}\boldsymbol{P}_{\boldsymbol{m}}\left(\boldsymbol{P}_{\boldsymbol{m}}^{\mathrm{T}}\boldsymbol{R}_{\boldsymbol{n}}^{-1}\boldsymbol{P}_{\boldsymbol{m}}\right)^{-1}\boldsymbol{P}_{\boldsymbol{m}}^{\mathrm{T}}\boldsymbol{R}_{\boldsymbol{n}}^{-1}\right]\hat{\boldsymbol{U}}_s=\boldsymbol{G}_a\hat{\boldsymbol{U}}_s \tag{48}$$

$$\boldsymbol{b}=\left(\boldsymbol{P}_{\boldsymbol{m}}^{\mathrm{T}}\boldsymbol{R}_{\boldsymbol{n}}^{-1}\boldsymbol{P}_{\boldsymbol{m}}\right)^{-1}\boldsymbol{P}_{\boldsymbol{m}}^{\mathrm{T}}\boldsymbol{R}_{\boldsymbol{n}}^{-1}\hat{\boldsymbol{U}}_s=\boldsymbol{G}_b\hat{\boldsymbol{U}}_s \tag{49}$$

thus, Eq. (38) can be rewritten as,

$$\begin{aligned}u^{\mathrm{h}}(\boldsymbol{x})&=\boldsymbol{R}^{\mathrm{T}}(\boldsymbol{x})\boldsymbol{a}+\boldsymbol{p}^{\mathrm{T}}(\boldsymbol{x})\boldsymbol{b}=\left[\boldsymbol{R}^{\mathrm{T}}(\boldsymbol{x})\boldsymbol{G}_a+\boldsymbol{p}^{\mathrm{T}}(\boldsymbol{x})\boldsymbol{G}_b\right]\hat{\boldsymbol{U}}_s\\&=\sum_{i=1}^{n}\varphi_i(x)\hat{u}_i=\boldsymbol{\Phi}(\boldsymbol{x})\hat{\boldsymbol{U}}_s\end{aligned} \tag{50}$$

in which the shape function is defined,

$$\boldsymbol{\Phi}(\boldsymbol{x})=\boldsymbol{R}^{\mathrm{T}}(x)\boldsymbol{G}_a+\boldsymbol{p}^{\mathrm{T}}(x)\boldsymbol{G}_b \tag{51}$$

The first two orders of derivatives of the form function in Eq. (51) are expressed as,

$$\begin{cases}\boldsymbol{\Phi}_{,i}(\boldsymbol{x})=\boldsymbol{R}_{,i}^{\mathrm{T}}(\boldsymbol{x})\boldsymbol{G}_a+\boldsymbol{p}_{,i}^{\mathrm{T}}(\boldsymbol{x})\boldsymbol{G}_b\\ \boldsymbol{\Phi}_{,ij}(\boldsymbol{x})=\boldsymbol{R}_{,ij}^{\mathrm{T}}(\boldsymbol{x})\boldsymbol{G}_a+\boldsymbol{p}_{,ij}^{\mathrm{T}}(\boldsymbol{x})\boldsymbol{G}_b\end{cases} \tag{52}$$

Another important issue that must be considered in meshfree methods is the selection of the radius of the support domain. As shown in Fig 6, for a computational node $\boldsymbol{x}_{\mathrm{Q}}$, the radius d_m of its support domain is determined by [59],

$$d_m=\alpha_c d_c \tag{53}$$

where d_c is a characteristic length related to the nodal spacing while α_c denotes the scale factor. According to conclusions from the literature [61], the optimal value of α_c is 2.4.

3.2 NSGT formulation based on RPIM

According to the RPIM shape function, the displacement field can be expressed as,

$$\begin{aligned}\boldsymbol{u}^{\mathrm{h}}(x,y)&=\sum_{i=1}^{n}\begin{bmatrix}\varphi_i(x,y)&0&0&0&0&0&0\\0&\varphi_i(x,y)&0&0&0&0&0\\0&0&\varphi_i(x,y)&0&0&0&0\\0&0&0&\varphi_i(x,y)&0&0&0\\0&0&0&0&\varphi_i(x,y)&0&0\\0&0&0&0&0&\varphi_i(x,y)&0\\0&0&0&0&0&0&\varphi_i(x,y)\end{bmatrix}\begin{Bmatrix}u_{0i}\\v_{0i}\\w_{0i}\\\psi_{xi}\\\psi_{yi}\\\phi_{xi}\\\phi_{yi}\end{Bmatrix}\\&=\sum_{i=1}^{n}\boldsymbol{\Phi}_i(x,y)\boldsymbol{q}_i\end{aligned}$$

(54)

where $\boldsymbol{q}_i$ is a displacement vector containing n support nodes and $\psi_{xi} = \partial w_0/\partial x$, $\psi_{yi} = \partial w_0/\partial y$.

Substituting Eq. (54) into Eq. (24), the bending and shear strains can be expressed in compact form as,

$$\bar{\boldsymbol{\varepsilon}} = \begin{Bmatrix} \boldsymbol{\varepsilon}_0 \\ \boldsymbol{\varepsilon}_1 \\ \boldsymbol{\varepsilon}_2 \end{Bmatrix} = \sum_{i=1}^{n} \begin{Bmatrix} \boldsymbol{B}_i^0 \\ \boldsymbol{B}_i^1 \\ \boldsymbol{B}_i^2 \end{Bmatrix} \boldsymbol{q}_i = \sum_{i-1}^{n} \bar{\boldsymbol{B}}_i^{\mathrm{b}} \boldsymbol{q}_i, \ \bar{\gamma} = \begin{Bmatrix} \boldsymbol{\varepsilon}_0^{\mathrm{s}} \\ \boldsymbol{\varepsilon}_1^{\mathrm{s}} \end{Bmatrix} = \sum_{i-1}^{n} \begin{Bmatrix} \boldsymbol{B}_i^{\mathrm{s}0} \\ \boldsymbol{B}_i^{\mathrm{s}1} \end{Bmatrix} \boldsymbol{q}_i = \sum_{i=1}^{n} \bar{\boldsymbol{B}}_i^{\mathrm{s}} \boldsymbol{q}_i \tag{55}$$

where

$$\boldsymbol{B}_i^0 = \begin{bmatrix} \varphi_{i,x} & 0 & 0 & 0 & 0 & \varphi_{i,x}A^k & 0 \\ 0 & \varphi_{i,y} & 0 & 0 & 0 & 0 & \varphi_{i,y}C^k \\ \varphi_{i,y} & \varphi_{i,x} & 0 & 0 & 0 & \varphi_{i,y}A^k & \varphi_{i,x}C^k \end{bmatrix}, \ \boldsymbol{B}_i^{\mathrm{s}0} = \begin{bmatrix} 0 & 0 & \varphi_{i,x} & -\varphi_i & 0 & \varphi_i B^k & 0 \\ 0 & 0 & \varphi_{i,y} & 0 & -\varphi_i & 0 & \varphi_i D^k \end{bmatrix},$$

$$\boldsymbol{B}_i^1 = \begin{bmatrix} 0 & 0 & 0 & -\varphi_{i,x} & 0 & \varphi_{i,x}B^k & 0 \\ 0 & 0 & 0 & 0 & -\varphi_{i,y} & 0 & \varphi_{i,y}D^k \\ 0 & 0 & 0 & -\varphi_{i,y} & -\varphi_{i,x} & \varphi_{i,y}B^k & \varphi_{i,x}D^k \end{bmatrix}, \ \boldsymbol{B}_i^{\mathrm{s}1} = \begin{bmatrix} 0 & 0 & 0 & 0 & 0 & \varphi_i & 0 \\ 0 & 0 & 0 & 0 & 0 & 0 & \varphi_i \end{bmatrix},$$

$$\boldsymbol{B}_i^2 = \begin{bmatrix} 0 & 0 & 0 & 0 & 0 & \varphi_{i,x} & 0 \\ 0 & 0 & 0 & 0 & 0 & 0 & \varphi_{i,y} \\ 0 & 0 & 0 & 0 & 0 & \varphi_{i,y} & \varphi_{i,x} \end{bmatrix}.$$

(56)

Similarly, substituting Eq. (54) into Eq. (22), the displacement component is expressed as,

$$\bar{\boldsymbol{u}} = \begin{Bmatrix} \boldsymbol{u}_0 \\ \boldsymbol{u}_1 \\ \boldsymbol{u}_2 \end{Bmatrix} = \sum_{i=1}^{n} \begin{Bmatrix} \boldsymbol{\Phi}_i^0 \\ \boldsymbol{\Phi}_i^1 \\ \boldsymbol{\Phi}_i^2 \end{Bmatrix} \boldsymbol{q}_i = \sum_{i=1}^{n} \bar{\boldsymbol{\Phi}}_i \boldsymbol{q}_i \tag{57}$$

where

$$\boldsymbol{\Phi}_i^0 = \begin{bmatrix} \varphi_i & 0 & 0 & 0 & 0 & \varphi_i A^k & 0 \\ 0 & \varphi_i & 0 & 0 & 0 & 0 & \varphi_i C^k \\ 0 & 0 & \varphi_i & 0 & 0 & 0 & 0 \end{bmatrix}, \quad \boldsymbol{\Phi}_i^1 = \begin{bmatrix} 0 & 0 & 0 & -\varphi_i & 0 & \varphi_i B^k & 0 \\ 0 & 0 & 0 & 0 & -\varphi_i & 0 & \varphi_i D^k \\ 0 & 0 & 0_i & 0 & 0 & 0 & 0 \end{bmatrix},$$

$$\boldsymbol{\Phi}_i^2 = \begin{bmatrix} 0 & 0 & 0 & 0 & 0 & \varphi_i & 0 \\ 0 & 0 & 0 & 0 & 0 & 0 & \varphi_i \\ 0 & 0 & 0_i & 0 & 0 & 0 & 0 \end{bmatrix} \tag{58}$$

Substituting Eqs. (55) and (57) into Eqs. (32) and (34), respectively, the discrete forms of the governing equations for bending and free vibration of the plate can be expressed as,

$$\boldsymbol{K}\boldsymbol{q} = \boldsymbol{f}, \quad \boldsymbol{K} = \boldsymbol{K}^{\mathrm{m}} + \boldsymbol{K}^{\mathrm{w}} \tag{59}$$

$$\left(\boldsymbol{K} - \omega^2 \boldsymbol{M}\right)\boldsymbol{q} = \boldsymbol{0} \tag{60}$$

where $\boldsymbol{K}$, $\boldsymbol{M}$ and $\boldsymbol{f}$ denote the global stiffness matrix, mass matrix and force vector, respectively; ω is intrinsic frequency. $\boldsymbol{K}^{\mathrm{m}}$ is the stiffness matrix for the deformation of the functional gradient plate, and $\boldsymbol{K}^{\mathrm{w}}$is the stiffness matrix for the elastic foundation, which are computed as, respectively,

$$\begin{aligned} \boldsymbol{K}^{\mathrm{m}} &= \int_\Omega \left(\bar{\boldsymbol{B}}^{\mathrm{b}}\right)^{\mathrm{T}} \boldsymbol{Q}^{\mathrm{b}} \bar{\boldsymbol{B}}^{\mathrm{b}} \mathrm{d}\Omega + \int_\Omega \left(\bar{\boldsymbol{B}}^{\mathrm{s}}\right)^{\mathrm{T}} \boldsymbol{Q}^{\mathrm{s}} \bar{\boldsymbol{B}}^{\mathrm{s}} d\Omega - \lambda \int_\Omega \left(\nabla^2 \bar{\boldsymbol{B}}^{\mathrm{b}}\right)^{\mathrm{T}} \boldsymbol{Q}^{\mathrm{b}} \bar{\boldsymbol{B}}^{\mathrm{b}} \mathrm{d}\Omega \\ &\quad -\lambda \int_\Omega \left(\nabla^2 \bar{\boldsymbol{B}}^{\mathrm{s}}\right)^{\mathrm{T}} \boldsymbol{Q}^{\mathrm{s}} \bar{\boldsymbol{B}}^{\mathrm{s}} \mathrm{d}\Omega \end{aligned} \tag{61}$$

$$\boldsymbol{K}^{\mathrm{w}} = \int_\Omega \left(1 - \mu\nabla^2\right)\left(\bar{\boldsymbol{B}}^{\mathrm{w}}\right)^{\mathrm{T}} K_{\mathrm{w}} \bar{\boldsymbol{B}}^{\mathrm{w}} \mathrm{d}\Omega \tag{62}$$

with

$$\bar{\boldsymbol{B}}^{\mathrm{w}} = \begin{bmatrix} 0 & 0 & \varphi_i & 0 & 0 & 0 & 0 \end{bmatrix} \tag{63}$$

General mass matrix is computed as:

$$\boldsymbol{M} = \int_\Omega \left(1 - \mu\nabla^2\right) \bar{\boldsymbol{\Phi}}^{\mathrm{T}} \boldsymbol{I}_{\mathrm{m}} \bar{\boldsymbol{\Phi}} \mathrm{d}\Omega \tag{64}$$

Force vector is computed as:

$$\boldsymbol{f} = \int_\Omega \left(1 - \mu\nabla^2\right) q_0 \begin{bmatrix} 0 & 0 & \varphi_i & 0 & 0 & 0 & 0 \end{bmatrix}^{\mathrm{T}} \mathrm{d}\Omega \tag{65}$$

To compute the integrals, boundary conditions are imposed on governing equations. Owing to the Kronecker delta function property of RPIM, the essential boundary conditions in present model are imposed easily and directly as in standard finite element method. In this paper, the boundary condition of simple four-sided support (SSSS) is taken as the main object of study. In contrast, the boundary condition of four-sided solid support (CCCC) and two-side free two-sided solid support (SCSC or CSCS) are taken as an additional object of study, as shown in Table 1.

Table 1. The boundary conditions for plates.

Type	Conditions	Values
SSSS	At $y = 0, b$ (S) At $x = 0, a$ (S)	$u = w_0 = \psi_x = \phi_x = 0$ $v = w_0 = \psi_y = \phi_y = 0$
CCCC	At all edges (C)	$u = v = w_0 = \psi_x = \psi_y = \phi_x = \phi_y = 0$
SCSC	At $y = 0, b$ (C) At $x = 0, a$ (S)	$u = v = w_0 = \psi_x = \psi_y = \phi_x = \phi_y = 0$ $v = w_0 = \psi_y = \phi_y = 0$
CSCS	At $y = 0, b$ (S) At $x = 0, a$ (C)	$u = w_0 = \psi_x = \phi_x = 0$ $u = v = w_0 = \psi_x = \psi_y = \phi_x = \phi_y = 0$

4. Numerical examples and discussions

In this study, the functionally graded materials are mixtures of aluminium (Al) as a metal and zirconium oxide (ZrO_2) as a ceramic. Unless otherwise specified, the material parameters utilized for subsequent examples are set to: $E_{\mathrm{m}} = 70$ GPa, $E_{\mathrm{c}} = 151$ GPa, $\rho_{\mathrm{m}} = 2700\ \mathrm{kg/m^3}$, $\rho_{\mathrm{c}} = 5680\ \mathrm{kg/m^3}$, $\nu_{\mathrm{m}} = \nu_{\mathrm{c}} = 0.3$. In addition, the normalisation parameters for all numerical results analysis are evaluated in the following form:

- Dimensionless central deflection:

$$\bar{w} = \frac{10hE_0}{a^2 q_0} w\left(\frac{a}{2}, \frac{b}{2}, \bar{z}\right) \tag{66}$$

where .

- Dimensionless axial stress:

$$\bar{\sigma}_{xx} = \frac{h^2}{a^2 q_0} \sigma_{xx}\left(\frac{a}{2}, \frac{b}{2}, \bar{z}\right) \tag{67}$$

- Dimensionless shear stress:

$$\bar{\tau}_{xz} = \frac{h}{aq_0} \tau_{xz}\left(0, \frac{b}{2}, \bar{z}\right) \tag{68}$$

$$\bar{\tau}_{xy} = \frac{10h^2}{a^2 q_0} \tau_{xy}\left(0, 0, \bar{z}\right) \tag{69}$$

- Dimensionless frequency:

$$\bar{\omega} = \omega h \sqrt{\frac{\rho_{\mathrm{c}}}{E_{\mathrm{c}}}} \tag{70}$$

4.1 Verification and comparison

Initially, to verify the correctness of RPIM in combination with GL-HSDT, nonlocal and strain gradient effects are ignored. A simply supported sandwich square plate proposed by Srinivas [62] under a uniform transverse load q_0 is considered, which has a ratio of face layer thickness h_f to core layer thickness h_c as $h_f/h_c = 1/8$. The material properties of face and core layers are determined as follow,

$$Q_{\text{core}} = \begin{bmatrix} 0.999781 & 0.231192 & 0 & 0 & 0 \\ 0.231192 & 0.524886 & 0 & 0 & 0 \\ 0 & 0 & 0.262931 & 0 & 0 \\ 0 & 0 & 0 & 0.266810 & 0 \\ 0 & 0 & 0 & 0 & 0.159914 \end{bmatrix}$$

$$Q_{\text{face}} = RQ_{\text{core}}$$

In this example, the square plate is modeled by a set of 17×17, 21×21 and 25×25 nodes, and the normalized displacements and stresses are as follows,

$$\begin{aligned} &\bar{w} = 0.999781 w\left(\frac{a}{2}, \frac{a}{2}, 0\right); \\ &\bar{\sigma}_{xx}^{(1)} = \sigma_{xx}^{(1)}\left(\frac{a}{2}, \frac{a}{2}, \frac{h}{2}\right)/q_0;\ \bar{\sigma}_{xx}^{(2)} = \sigma_{xx}^{(1)}\left(\frac{a}{2}, \frac{a}{2}, \frac{2h}{5}\right)/q_0;\ \bar{\sigma}_{xx}^{(3)} = \sigma_{xx}^{(2)}\left(\frac{a}{2}, \frac{a}{2}, \frac{2h}{5}\right)/q_0; \\ &\bar{\sigma}_{yy}^{(1)} = \sigma_{yy}^{(1)}\left(\frac{a}{2}, \frac{a}{2}, \frac{h}{2}\right)/q_0;\ \bar{\sigma}_{yy}^{(2)} = \sigma_{yy}^{(1)}\left(\frac{a}{2}, \frac{a}{2}, \frac{2h}{5}\right)/q_0;\ \bar{\sigma}_{yy}^{(3)} = \sigma_{yy}^{(2)}\left(\frac{a}{2}, \frac{a}{2}, \frac{2h}{5}\right)/q_0; \end{aligned}$$

Table 2 provides a comparison between the present solution and the exact solution reported by Srinivas [60], HSDT-based finite element solution of Pandya and Kant [61], the HSDT-based meshless solution of Ferreira et al. [62] and the closed-form solution based on inverse hyperbolic shear deformation theory (iHSDT) by Grover et al. [63]. It can be seen that the present results are nearly identical to the exact solution reported by Srinivas. Particularly, for the case of R =15, the accuracy of our solution significantly surpasses that of other HSDT-based solutions, which highlights the advantages of GL-HSDT in dealing with sandwich structures. Moreover, it can be observed that the accuracy of computed results improves as the node density increases, successfully demonstrating the convergency of present model using the RPIM. Considering the balance between computational cost and accuracy, a set of 21×21 nodes is used for subsequent analysis and comparison.

Next, the nonlocal parameter μ and strain gradient parameter λ are introduced by NSGT to validate the effectiveness of developed model in examining size-scale effects. By referring to the parameter values recommended in existing literature, we choose those utilized by Daikh et al. [46], applying them to the model for computation. As shown in Table 3, the dimensionless central deflections of FGSNPs are computed for the nonlocal effect and strain gradient effect, which are compared with the results reported by Daikh et al. It is clear that the present results are in good agreement with those of the reference solution. This further demonstrates the correctness of the model to provide reliable predictions for microscopic effects.

Table 2. Dimensionless displacement and stresses of the sandwich square plate under uniform load. (SSSS, $a/h = 10, \mu = \lambda = 0$)

R	Method	$\bar{w}$	$\bar{\sigma}_{xx}^{(1)}$	$\bar{\sigma}_{xx}^{(2)}$	$\bar{\sigma}_{xx}^{(3)}$	$\bar{\sigma}_{yy}^{(1)}$	$\bar{\sigma}_{yy}^{(2)}$	$\bar{\sigma}_{yy}^{(3)}$
5	FEM-HSDT [63]	256.13	62.38	46.91	9.382	38.93	30.33	6.065
	Meshfree-HSDT [64]	257.11	60.366	47.003	9.401	38.456	30.242	6.048
	CFS-iHSDT [65]	255.644	60.675	47.055	9.411	38.522	30.206	6.041
	Exact [62]	258.97	60.353	46.623	9.34	38.491	30.097	6.161
	Present (17×17)	**257.2691**	**59.7455**	**46.5821**	**9.0121**	**37.8472**	**29.7463**	**5.8838**
	Present (21×21)	**257.9246**	**60.0124**	**47.1356**	**9.3543**	**38.3561**	**30.0355**	**6.1613**
	Present (25×25)	**258.3055**	**60.2156**	**47.3237**	**9.3872**	**38.5218**	**30.1474**	**6.2467**
10	FEM-HSDT [63]	152.33	64.65	51.31	5.131	42.83	33.97	3.397
	Meshfree-HSDT [64]	154.658	65.381	49.973	4.997	43.24	33.637	3.364
	CFS-iHSDT [65]	154.55	65.741	49.798	4.979	43.4	33.556	3.356
	Exact [62]	159.38	65.332	48.857	4.903	43.566	33.413	3.5
	Present (17×17)	**157.7876**	**64.6521**	**47.8846**	**4.5251**	**43.0457**	**33.0146**	**3.1025**
	Present (21×21)	**158.4561**	**65.2872**	**48.6543**	**4.8103**	**43.5374**	**33.4051**	**3.5465**
	Present (25×25)	**158.6233**	**65.3136**	**48.7127**	**4.9857**	**43.5788**	**33.5141**	**3.6451**
15	FEM-HSDT [63]	110.43	66.62	51.97	3.465	44.92	35.41	2.361
	Meshfree-HSDT [64]	114.644	66.919	50.323	3.355	45.623	35.167	2.345
	CFS-iHSDT [65]	115.82	67.272	49.813	3.321	45.967	35.088	2.339
	Exact [62]	121.72	66.787	48.299	3.238	46.424	34.955	2.494
	Present (17×17)	**120.7152**	**66.0548**	**47.8463**	**3.0542**	**46.0725**	**34.6497**	**2.1024**
	Present (21×21)	**121.2054**	**66.4671**	**48.2334**	**3.2136**	**46.4231**	**34.8526**	**2.4673**
	Present (25×25)	**121.5437**	**66.5137**	**48.4103**	**3.3357**	**46.5332**	**34.9543**	**2.5451**

Table 3. Comparison of dimensionless central deflections of square FGSNPs for several nonlocal and strain gradient parameters. ($SSSS, a/h = 10, p = 2$).

μ	λ	Type					
		1-1-1		1-2-1		2-2-1	
		Daikh [46]	**Present**	Daikh [46]	**Present**	Daikh [46]	**Present**
0	0	0.29777	**0.29789**	0.27308	**0.27051**	0.28494	**0.27756**
	1	0.24868	**0.24742**	0.22806	**0.22468**	0.23797	**0.23468**
	2	0.21349	**0.20723**	0.19579	**0.18817**	0.20429	**0.19656**
1	0	0.35655	**0.35394**	0.32698	**0.32130**	0.34119	**0.33566**
	1	0.29777	**0.29789**	0.27308	**0.27051**	0.28494	**0.27756**
	2	0.25563	**0.25415**	0.23443	**0.23079**	0.24462	**0.24106**
2	0	0.41533	**0.41484**	0.38089	**0.37658**	0.39743	**0.39342**
	1	0.34686	**0.34903**	0.31810	**0.31712**	0.33192	**0.33111**
	2	0.29777	**0.29789**	0.27308	**0.27051**	0.28494	**0.27756**

4.2 Parametric study

In this section, firstly, the macroscopic mechanical behaviours of TFGNPs are examined for various condition parameters through bending and vibration analysis. Here, the nonlocal and strain gradient parameters are set to zero to make the present model revert to a classical elasticity theory model, which is utilized to obtain results for the macroscopic counterparts. Then considering the size-scale effects of nanostructures, the influence of the nonlocal and strain gradient parameters on the static bending and free vibration of TFGNPs was investigated.

4.2.1 Static bending analysis

In order to show the advantages of TFGNPs, we compare their stress variations with those of conventional FGSNPs. As shown in Fig. 7, the axial and shear stresses of FGNPs along the thickness vary with the power-law exponent p. It is observed that when p = 5, there is a significant abrupt change in stress at the interface between the core and surface layers. The situation is further aggravated when p = 10. Fig. 8 displays the variation of dimensionless axial and shear stresses along the thickness of TFGNP-A, with the parameter N ranging from 1 to 3. Similarly, the variation of dimensionless stresses in TFGNP-B is presented in Fig. 9. It is clear that the proposed TFGNPs possesses extreme continuous and smooth stress variation over the entire thickness, which is attributed to its material gradation in each layer described by a unified cosine function.

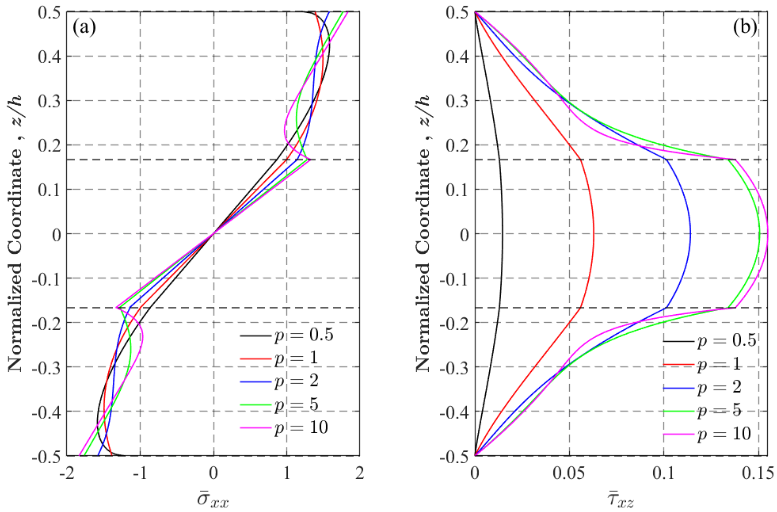

Fig. 7 Dimensionless stresses along the thickness of square FGSNPs. (SSSS, $a/h = 10, k_w = \mu = \lambda = 0$).

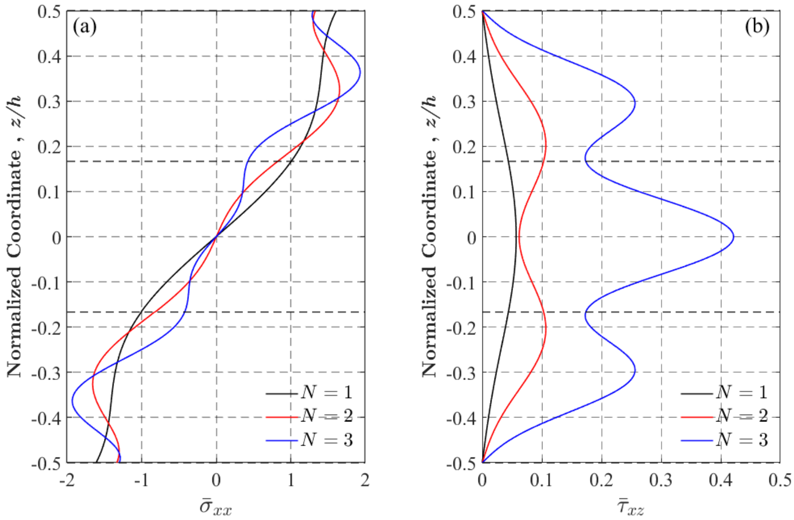

Fig. 8 Dimensionless stresses along the thickness of square TFGNP-A. (SSSS, $a/h = 10, k_w = \mu = \lambda = 0$).

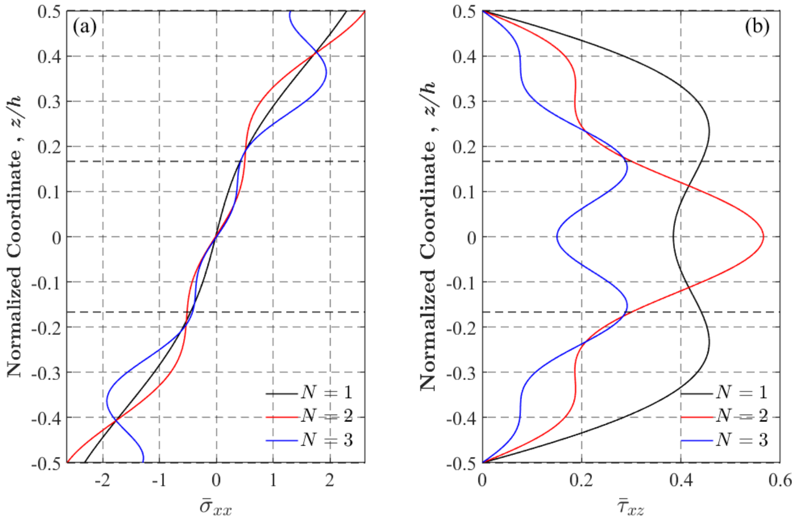

Fig. 9 Dimensionless stresses along the thickness of square TFGNP-B. (SSSS, $a/h = 10, k_{\mathrm{w}} = \mu = \lambda = 0$).

Fig. 10 displays the dimensionless central deflection of TFGNPs as affected by the parameter N. It can be seen that for TFGNP-A, the maximum deflection occurs at N = 1 and then decreases sharply up to N = 2. Continuing to increase N, the decrease in deflection slows down until it eventually remains constant. Reviewing Fig. 5(a), we find that the content of ceramic in core layer of TFGNP-A far exceeds that of the surface layers at N = 1, while things are reversed at N = 2. When N increases to 3, the ceramic content becomes equal among the layers, although the ceramic contents of surface layers are less than that at N = 2. The opposite is true for TFGNP-B in Fig. 5(b). Combining Figs. 5 and 10, we can explain this by noting that the higher elastic modulus of ceramics compared to metals means that when ceramics are concentrated in the surface layers of TFGNPs, it leads to enhanced bending stiffness of the plate, resulting in lower deflection. In addition, achieving a uniform distribution of ceramics among the layers further enhances the overall stiffness of the plate, thereby reducing deflection.

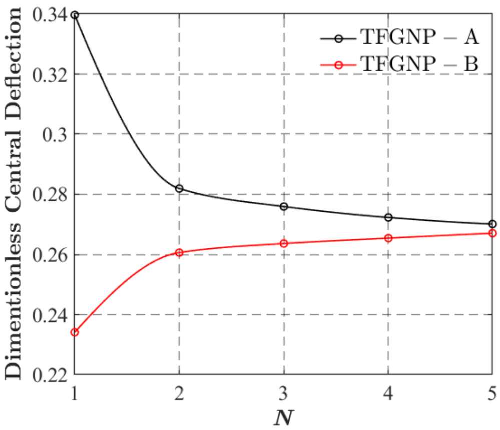

Fig. 10 Effect of parameter N on the dimensionless central deflection of square TFGNPs. (SSSS, $a/h = 10, k_{\mathrm{w}} = \mu = \lambda = 0$).

Table 4 presents dimensionless stresses for various values of parameter N. It is obvious that the effect of increasing or decreasing N on the stresses of TFGNPs is significantly weakened when N is above 1. In combination with Fig. 10, a stable material property of TFGNPs can be demonstrated. Further, Table 5 offers insights into the influence of boundary conditions and width-to-thickness ratio on their central deflection. It can be seen that TFGNPs achieve minimum deflection with four-sided clamped, while an increase in width-to-thickness ratio serves to raise the deflection of plates.

Table 4. Dimensionless stresses of square TFGNPs for several parameters N. (SSSS, $a/h = 10, k_{\mathrm{w}} = \mu = \lambda = 0$).

N	TFGNP-A			TFGNP-B		
	$\bar{\sigma}_{xx}(h/2)$	$\bar{\tau}_{xy}(-h/2)$	$\bar{\tau}_{xz}(0)$	$\bar{\sigma}_{xx}(h/2)$	$\bar{\tau}_{xy}(-h/2)$	$\bar{\tau}_{xz}(0)$
1	1.61279	0.68656	0.05703	1.13248	0.48545	0.82978
2	1.33210	0.58012	0.13386	1.26060	0.54061	0.56583
3	1.31503	0.58822	0.42145	1.24481	0.54941	0.32472
4	1.27530	0.55627	0.12937	1.32446	0.56786	0.65624

Table 5. Dimensionless centre deflection of square TFGNPs with different boundary conditions edge-to-thickness ratios and parameters N. ($k_{\mathrm{w}} = \mu = \lambda = 0$).

BCs	a/h	TFGNP-A				TFGNP-B			
		$N = 1$	$N = 2$	$N = 3$	$N = 4$	$N = 1$	$N = 2$	$N = 3$	$N = 4$
SSSS	10	0.33966	0.28193	0.27594	0.27211	0.23410	0.26061	0.26262	0.27054
	20	1.32106	1.08977	1.05828	1.04418	0.85856	0.98356	1.00716	1.02489
	30	2.95573	2.43530	2.36125	2.33274	1.89824	2.18745	2.24718	2.27841
CCCC	10	0.13006	0.10963	0.10913	0.10559	0.10078	0.10643	0.10392	0.11143
	20	0.47815	0.39638	0.38694	0.38025	0.32347	0.36351	0.36835	0.37919
	30	1.05597	0.87231	0.84786	0.83609	0.69165	0.78953	0.80708	0.82273
SCSC	10	0.18201	0.15286	0.15158	0.14710	0.13734	0.14677	0.14433	0.15356
	20	0.67848	0.56175	0.54763	0.53872	0.45442	0.51309	0.52129	0.53508
	30	1.50339	1.24109	1.20552	1.18937	0.97971	1.12107	1.14748	1.16807
CSCS	10	0.18199	0.15285	0.15156	0.14709	0.13732	0.14674	0.14431	0.15354
	20	0.67845	0.56173	0.54761	0.53870	0.45439	0.51306	0.52127	0.53505
	30	1.50334	1.24105	1.20548	1.18933	0.97967	1.12103	1.14744	1.16803

Table 6 examines the effect of foundation parameters on the centre deflection of TFGNPs, which show that an increase in both κ and ξ leads to a reduction in deflection, but the impact of κ is greater as compared to ξ. Furthermore, Fig. 11 portrays the deflection curves of TFGNPs with various foundations. The incorporation of elastic foundations is evident in reducing plate deflection, with minimal variation observed across different foundation types. This can be understood that although foundations enhance the stiffness of plates, their contribution to stiffness is considerably minor when compared to the inherent stiffness of TFGNPs, resulting in almost identical effects caused by different foundations.

Table 6. Effect of several Winkler foundation parameters on the central deflection of square TFGNPs (SSSS, $N = 1, a/h = 10, \mu = \lambda = 0$)

Type	κ	ξ	Linear	Parabolic	Reverse Parabolic	Sinusoidal	Reverse Sinusoidal
TFGNP-A	10	10	0.31730	0.32038	0.31428	0.31480	0.31983
		100	0.26519	0.28839	0.24542	0.24871	0.28406
		1000	0.10223	0.14945	0.07754	0.08120	0.13903
	100	10	0.22745	0.22904	0.22589	0.22616	0.22876
		100	0.19936	0.21223	0.18795	0.18987	0.20987
		1000	0.09058	0.12585	0.07062	0.07363	0.11834
	1000	10	0.05937	0.05948	0.05926	0.05928	0.05946
		100	0.05726	0.05830	0.05625	0.05643	0.05811

		1000	0.04242	0.04894	0.03740	0.03822	0.04771
TFGNP-B	10	10	0.22326	0.22478	0.22175	0.22202	0.22451
		100	0.19611	0.20853	0.18507	0.18693	0.20625
		1000	0.08969	0.12394	0.07016	0.07310	0.11661
	100	10	0.17470	0.17563	0.17377	0.17394	0.17547
		100	0.15762	0.16557	0.15039	0.15162	0.16412
		1000	0.08062	0.10732	0.06446	0.06693	0.10175
	1000	10	0.05503	0.05512	0.05493	0.05495	0.05510
		100	0.05321	0.05410	0.05234	0.05249	0.05394
		1000	0.04013	0.04591	0.03563	0.03636	0.04482

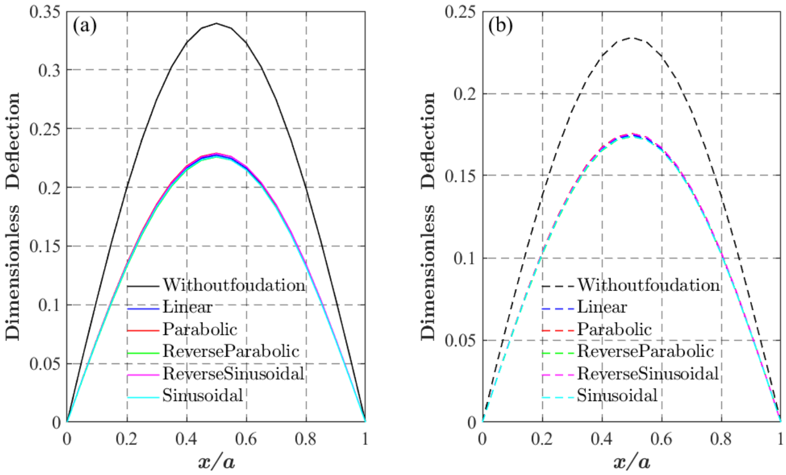

Fig. 11 Effect of different Winkler foundations on the central deflection of square TFGNPs: (a)TFGNP-A; (b)TFGNP-B. (SSSS, $\kappa = 100, \xi = 10, N = 1, a/h = 10, \mu = \lambda = 0$)

4.2.2 Free vibration response

In this subsection, we investigate the free vibration response of TFGNPs under various parameters. Fig. 12 illustrates the effect of parameter N on the first dimensionless frequency, where the maximum frequency of TFGNPs occurs in TFGNP-B at $N = 1$. Referring to Fig. 5(b), it is observed that the ceramic content of surface layers of TFGNP-B far exceeds that of the core layer at $N = 1$, which leads to an enhanced stiffness of the plate and hence a higher vibration frequency. This further supports our previous analysis. Moreover, in combination with Figs. 10 and 12, we can conclude that TFGNP-B has higher stiffness than TFGNP-A.

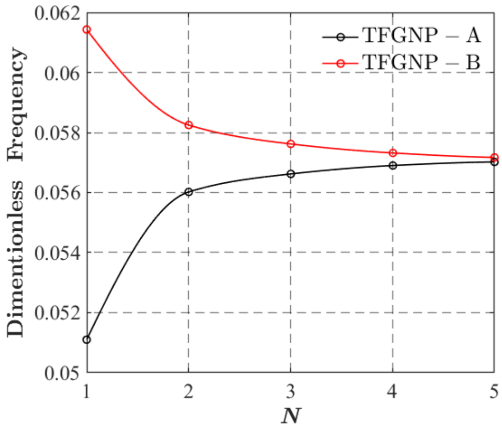

Fig. 12 Effect of parameter N on the first dimensionless frequency of square TFGNPs. (SSSS, $a/h = 10, k_w = \mu =$

$\lambda = 0$).

Considering two types of boundary conditions, simply supported (SSSS) and four-sided clamped (CCCC), the first six dimensionless frequencies for several aspect ratios are presented in Table 7. It is shown that higher frequency occurs for the CCCC while increasing the aspect ratio of plates lowers the frequency, which is consistent with the results reported by Phan-Dao [23] and Thai [22] et al. This is attributed to the fact that the clamped approach imposes finer constraints on TFGNPs, consequently boosting the stiffness of the plate. In contrast, an increase in the aspect ratio causes bending stiffness of the longer side in the plate to decrease, resulting in a lower frequency.

Table 7. The first six dimensionless vibration frequency of TFGNPs with different boundary conditions and aspect ratios. ($N = 1, a/h = 10,, k_w = \mu = \lambda = 0$)

Bcs	Type	b/a	ω_1	ω_1	ω_1	ω_1	ω_1	ω_1
SSSS	TFGNP-A	1	0.05110	0.12390	0.12390	0.19153	0.19339	0.19339
		2	0.03223	0.05111	0.08236	0.09679	0.10615	0.12336
		3	0.02869	0.03707	0.05114	0.06449	0.07100	0.09648
	TFGNP-B	1	0.06143	0.14186	0.14186	0.19339	0.19339	0.21128
		2	0.03932	0.06144	0.09679	0.09683	0.12288	0.14127
		3	0.03511	0.04504	0.06147	0.06449	0.08412	0.11236
CCCC	TFGNP-A	1	0.08915	0.17386	0.17386	0.24560	0.29455	0.29707
		2	0.06197	0.07955	0.11126	0.15331	0.15607	0.16835
		3	0.05856	0.06490	0.07705	0.09587	0.12119	0.15005
	TFGNP-B	1	0.10021	0.18531	0.18531	0.25440	0.29842	0.30141
		2	0.07115	0.09056	0.12467	0.16488	0.17104	0.18037
		3	0.06736	0.07443	0.08797	0.10860	0.13571	0.16156

Fig. 13 reveals the correlation between the Winkler dimensionless foundation parameter K_w and the first four vibration frequencies of TFGNP-A with CCCC boundary condition. As shown, the effects of foundation parameters on the first four vibration frequencies are in growth as $\log(K_w)$ equal to 2 and 3, while continuing to increase K_w has no effect on the vibration frequencies when $\log(K_w)$ equals to 5. Fig. 14 shows the first six vibration modes of TFGNP-A for CCCC boundary conditions with $\log(K_w)$ equal to 2, 3 and 5. It is clear that when the $\log(K_w)$ increased to 5, a chaotic vibration mode emerges in the plate structure. The findings derived from Figs. 13 and 14 lead to the conclusion that when increasing K_w reaches a certain critical value, further increments in K_w do not alter the frequency amplitude. On the contrary, excessive foundation stiffness will lead to vibration mode failure.

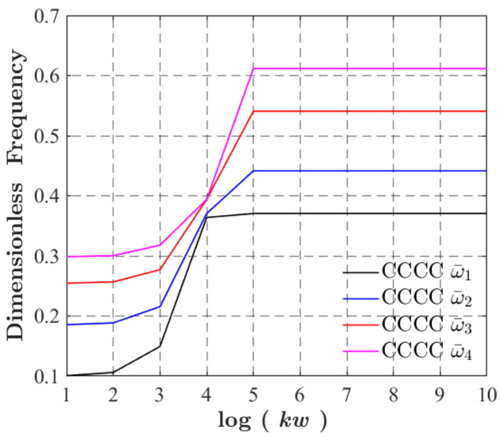

Fig. 13 Effect of Winkler foundation parameters on the first four dimensionless frequencies of square TFGNP-A with different CCCC boundary condition. $(N = 1, a/h = 10, \mu = \lambda = 0)$.

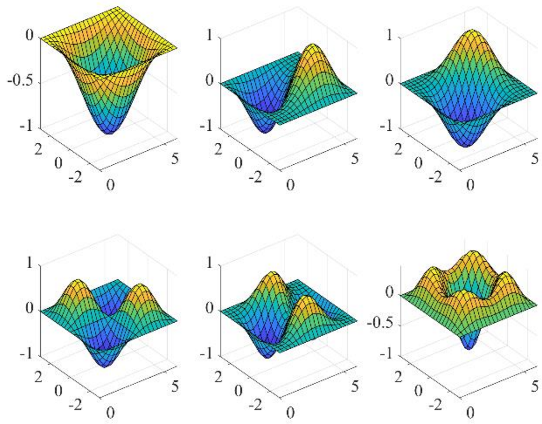

(a) $\log(K_{\mathrm{w}}) = 2$

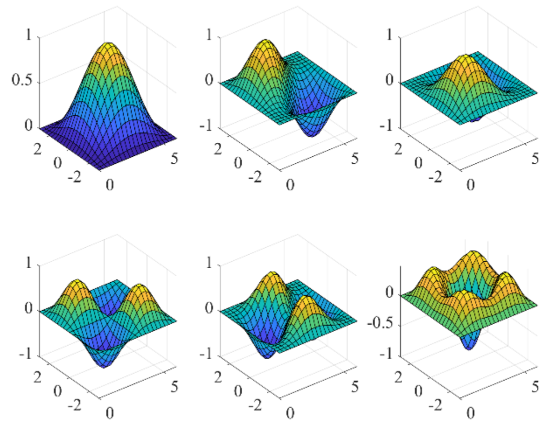

(b) $\log(K_{\mathrm{w}}) = 3$

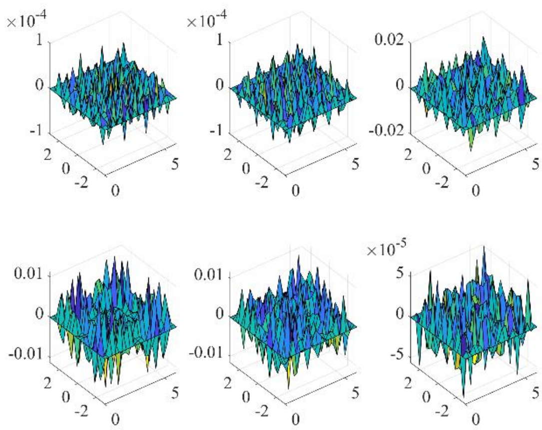

(c) $\log(K_{\mathrm{w}}) = 5$

Fig. 14 Effect of Winkler foundation parameters on the first six vibration modes of square TFGNP-A with CCCC boundary condition. ($N = 1, a/h = 10, \mu = \lambda = 0$).

It can be understood that when the foundation stiffness is excessive, the physical response of structures drastically varies on a very small scale. This non-uniform variation leads to an increase in the condition number of stiffness matrix, making the matrix pathological. As a result, the solved vibration modes are pseudo-modes that have no physical meaning. However, this challenge could be addressed by increasing the density of nodes in the computational domain and adjusting the weights to avoid pathological matrix during the solving process.

4.2.3 Size-scale effect

In this step, a study is dedicated to examining the impacts of nonlocal and strain gradient effects on the bending and free vibration of TFGNPs. Tables 8 and 9 provide the dimensionless central deflections and the first dimensionless vibration frequency for several sets of nonlocal and strain gradient parameters, respectively. It is obvious that the nonlocal and strain gradient parameters have a strong influence on the stiffness of plates and thus an important effect on the mechanical responses of plates.

Table 8. Dimensionless central deflection of square TFGNPs for several nonlocal and strain gradient parameters. (SSSS, $a/h = 10, k_{\mathrm{w}} = 0$).

μ	λ	TFGNP-A				TFGNP-B			
		$N=1$	$N=2$	$N=3$	$N=4$	$N=1$	$N=2$	$N=3$	$N=4$
0	0	0.33966	0.28193	0.27594	0.27211	0.23410	0.26061	0.26262	0.27054
	1	0.28108	0.23424	0.23027	0.22499	0.19951	0.21919	0.21926	0.22908
	2	0.24531	0.20434	0.20079	0.19626	0.17354	0.19102	0.19112	0.19958
1	0	0.40435	0.33562	0.32849	0.32393	0.28416	0.31024	0.31263	0.32206
	1	0.33987	0.28323	0.27844	0.27204	0.23544	0.26512	0.26503	0.27700
	2	0.28024	0.23344	0.22937	0.22420	0.19825	0.21822	0.21833	0.22799
2	0	0.46211	0.38356	0.37541	0.37020	0.33242	0.35456	0.35729	0.36807
	1	0.39757	0.33131	0.32571	0.31823	0.28220	0.31013	0.31003	0.32402
	2	0.34270	0.28546	0.28049	0.27416	0.24243	0.26686	0.26699	0.27880

Table 9. The first dimensionless nature frequency of square TFGNPs for several nonlocal and strain gradient parameters. (SSSS, $a/h = 10, k_{\mathrm{w}} = 0$).

μ	λ	TFGNP-A					TFGNP-B			
		$N=1$	$N=2$	$N=3$	$N=4$		$N=1$	$N=2$	$N=3$	$N=4$
0	0	0.05110	0.05602	0.05662	0.05717	0.06143	0.05825	0.05802	0.05802	0.05110
	1	0.06989	0.07643	0.07703	0.07795	0.08247	0.07884	0.07893	0.07715	0.06989
	2	0.08868	0.09684	0.09744	0.09873	0.10350	0.09943	0.09984	0.09628	0.08868
1	0	0.04108	0.04504	0.04552	0.04596	0.04938	0.04683	0.04664	0.04584	0.04108
	1	0.05616	0.06142	0.06190	0.06264	0.06624	0.06334	0.06342	0.06199	0.05616
	2	0.07125	0.07780	0.07828	0.07932	0.08310	0.07986	0.08020	0.07813	0.07125
2	0	0.03530	0.03871	0.03912	0.03950	0.04344	0.04025	0.04009	0.03940	0.03530
	1	0.04826	0.05278	0.05319	0.05383	0.05691	0.05443	0.05450	0.05326	0.04826
	2	0.06122	0.06685	0.06725	0.06815	0.07137	0.06860	0.06890	0.06712	0.06122

For a better presentation of these effects, Figs. 15 and 16 show the variation of bending and vibration with nonlocal and strain gradient parameters, respectively. In Fig. 15, the nonlocal dimensionless deflection ratio and dimensionless frequency ratio are defined as the ratios of the deflection and frequency predicted by nonlocal results ($\mu \neq$

$0, \lambda = 0)$ to the corresponding values predicted by the local results $(\lambda = \mu = 0)$, respectively. It is observed that the deflection ratio is over 1 while the frequency ratio is below 1. This means that the local theory underestimates the deflection and overestimates the intrinsic frequency of the TFGNPs compared to nonlocal theory. Particularly, the deflection and frequency further increase and decrease with increasing μ, respectively. Moreover, it can be seen that the nonlocal effects perform more dramatically for the CCCC boundary condition, and that the deflection ratio varies nonlinearly with nonlocal parameters. Similarly, the strain gradient dimensionless deflection ratios and dimensionless frequency ratios are defined as the ratios of the deflections and frequencies obtained only by considering the strain gradient effect $(\mu = 0, \lambda \neq 0)$ to the corresponding values obtained by neglecting the size-scale effect $(\lambda = \mu = 0)$, and that results are plotted in Fig. 16. It can be noticed that the effect of strain gradient effect on both deflection and frequency is exactly opposite to the conclusion drawn by considering the nonlocal effect.

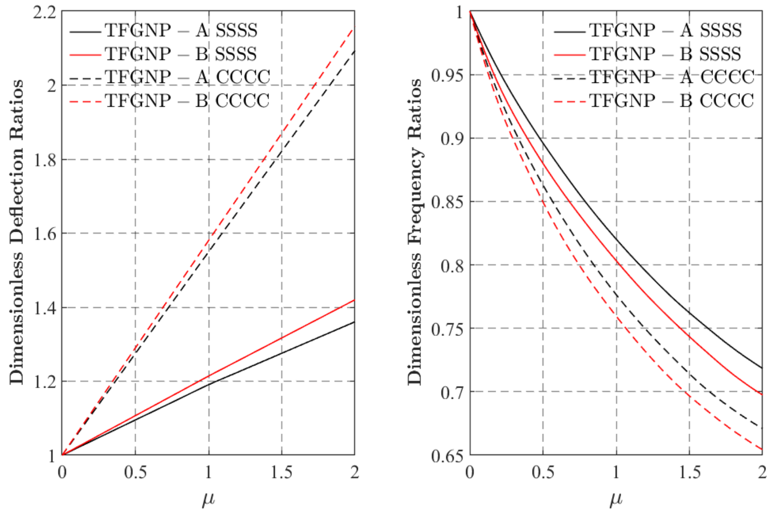

Fig. 15 Effect of nonlocal parameter on the dimensionless deflection and vibration frequency ratios for square TFGNPs. $(N = 1, a/h = 10, k_{\mathrm{w}} = 0)$.

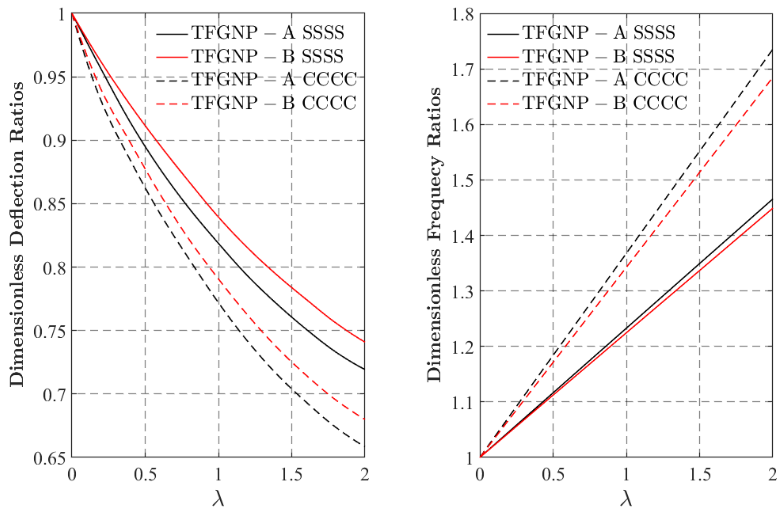

Fig. 16 Effect of strain gradient parameter on the dimensionless deflection and vibration frequency ratios for square TFGNPs. ($N = 1, a/h = 10, k_{\mathrm{w}} = 0$).

Fig. 17 shows the effect of nonlocal and strain gradient parameters on the axial stresses of TFGNPs. It can be seen that the axial stresses along the thickness distribution exhibit decrease and increase with increasing μ and λ, respectively. Also, the results on the shear stress of TFGNPs as affected by nonlocal and strain gradient parameters are posed in Fig. 18. The results demonstrate that the shear stresses along the thickness distribution increase with both μ and λ increasing. Our numerical findings demonstrate that through the modification of both parameters μ and λ using our proposed model based on NSGT, it is possible to unveil the mechanisms of plate stiffness softening and stiffness hardening.

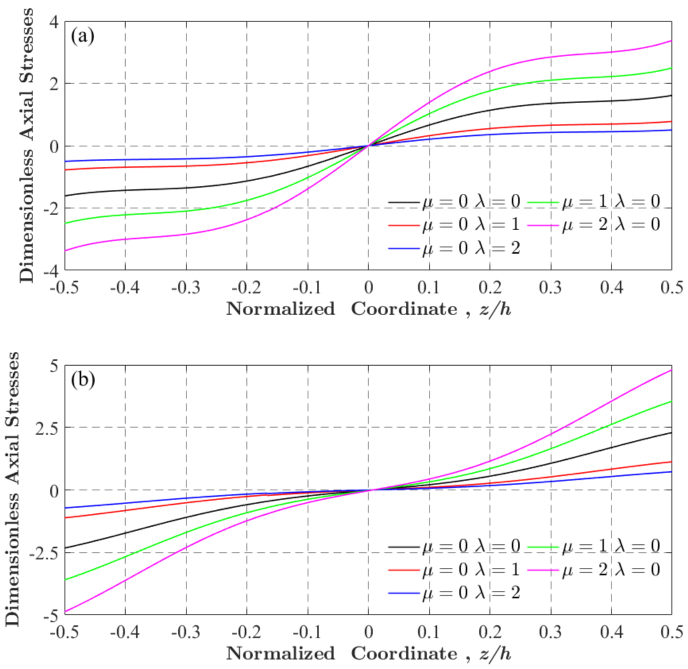

Fig. 17 Effect of nonlocal and strain gradient parameters on dimensionless axial stresses in square TFGNPs: (a)TFGNP-A; (b)TFGNP-B. (SSSS, $N = 1, a/h = 10, k_{\mathrm{w}} = 0$)

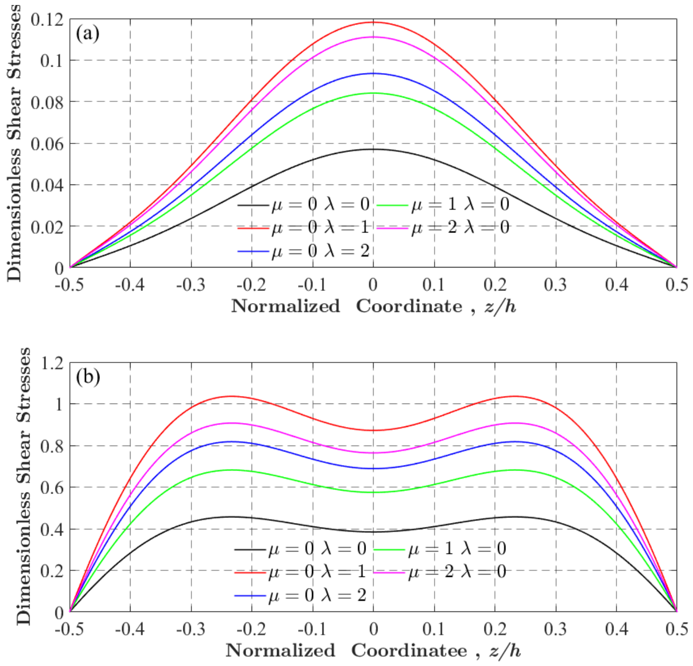

Fig. 18 Effect of nonlocal and strain gradient parameters on dimensionless shear stresses in square TFGNPs: (a)TFGNP-A; (b)TFGNP-B. (SSSS, $N = 1, a/h = 10, k_{\mathrm{w}} = 0$)

5. Conclusion

In this paper, the governing equations for FG plates are derived employing the GL-HSDT and weak-form NSGT. Then an effective size-dependent meshfree model is developed in combination with RPIM. In addition, we propose a novel trigonometric functionally graded nanoplates (TFGNPs) for the first time and consider the role of variable elastic foundations. The numerical results show that:

- Compared with finite element and meshfree models based on HSDT, the present model employing the generalized layerwise theory achieves more accurate computation for sandwich structures. Furthermore, in combination with NSGT, the physical behaviour of structures at micro and nano scales can be investigated effectively. The proposed TFGNPs achieve a perfect mixture between ceramics and metals for stable material properties compared to the traditional FGSNPs. Moreover, a continuous and smooth variation of axial and shear stresses along the thickness distribution shows its superior mechanical properties.

- Variation in parameter N affects the ceramics distribution along the thickness of TFGNPs. Increasing the ceramic content of surface layers leads to an increase in the stiffness of plates, and achieving a uniform distribution of ceramics across the layers further enhances the overall stiffness of plates.

- Increasing the nonlocal parameter decreases the stiffness of TFGNPs, therefore decrement in frequencies and an increment in deflections, while the opposite is found when increasing strain gradient parameter.

- The size-scale effects of TFGNPs show that the axial stresses along the thickness distribution decrease and increase with the growth of nonlocal and strain gradient parameters, respectively, but shear stresses along the thickness distribution adjust in direct proportion to the variations in the nonlocal and length scale parameters.

Notably, the model has certain limitations, primarily related to the distribution of nodes and the selection of weights, both of which can affect its numerical stability. For instance, excessive foundation stiffness induces numerical instability during computation and hence failure of vibration models. However, this challenge can be addressed by increasing the node density and adjusting the weights for the model.

In conclusion, despite some flaws, the model developed in this paper provides a high precision tool for a comprehensive observation of the complex mechanical behaviour of nanoplates across both macroscopic to microscopic scales. Additionally, the proposed TFGNPs possess excellent mechanical properties, demonstrating their potential for engineering applications.

Acknowledgements

This work was funded by the Key R&D Projects of Hunan Province (No.2024AQ2018); the open fund of Shanghai High Performance Fibers and Composites Center and Center for Civil Aviation Composites, Donghua University, 2024; the 2023 Hunan Province Transportation Science and Technology Progress and Innovation Project (202305); the Henan Province Science and Technology Key Research Project (242102521034); the Hunan Provincial Natural Science Foundation Project (No. 2024JJ9067); Key Scientific Research Project of Hunan Provincial Department of Education, Project (21A0073), Taishan Program (tsqn202306278); Open fund of Anhui Provincial Key Laboratory of Advanced Building Materials (Engineering Laboratory, International Joint Research Center) Project (NO.202206).

Declaration of Competing Interest

The authors declare that they have no known competing financial interests or personal relationships that could have appeared to influence the work reported in this paper.

Data Availability Statement

The data that support the findings of this study are available from the corresponding author, upon reasonable request.

References

[1] R. Jahanbazi, Y. Kiani, Y.T. Beni, Free vibration behaviour of composite laminated skew cylindrical shells reinforced with graphene platelets, Structures 61 (2024) 106074. https://doi.org/10.1016/j.istruc.2024.106074.

[2] M. Shen, Q. Wang, R. Wang, Investigation on the vibration mechanisms of a rotating FG-GPLRC shaft-disk-shell combined system, Structures 56 (2023) 105049. https://doi.org/10.1016/j.istruc.2023.105049.

[3] X. He, Z. Xiong, C. Lei, Z. Shen, A. Ni, Y. Xie, C. Liu, Excellent microwave absorption performance of LaFeO3/Fe3O4/C perovskite composites with optimized structure and impedance matching, Carbon 213 (2023) 118200. https://doi.org/10.1016/j.carbon.2023.118200.

[4] J. Dong, Y. Liu, S. Yuan, K. Li, F. Zhang, Z. Guan, H.K. Chai, Q. Wang, Mechanical behavior and impact resistance of rubberized concrete enhanced by basalt fiber-epoxy resin composite, Constr. Build. Mater. 435 (2024) 136836. https://doi.org/10.1016/j.conbuildmat.2024.136836.

[5] K. Liu, S. Zong, Y. Li, Z. Wang, Z. Hu, Z. Wang, Structural response of the U-type corrugated core sandwich panel used in ship structures under the lateral quasi-static compression load, Mar. Struct. 84 (2022) 103198. https://doi.org/10.1016/j.marstruc.2022.103198.

[6] Q. Cen, Z. Xing, Q. Wang, L. Li, Z. Wang, Z. Wu, L. Liu, Molding simulation of airfoil foam sandwich structure and interference optimization of foam-core, Chinese J. Aeronaut. (2024) S1000936124003315. https://doi.org/10.1016/j.cja.2024.08.025.

[7] C. Yang, Z. Li, P. Xu, H. Huang, Recognition and optimisation method of impact deformation patterns based on point cloud and deep clustering: Applied to thin-walled tubes, J. Ind. Inf. Integr. 40 (2024) 100607. https://doi.org/10.1016/j.jii.2024.100607.

[8] S. Benounas, M.-O. Belarbi, P. Van Vinh, A.A. Daikh, N. Fantuzzi, Finite element model for free vibration analysis of functionally graded doubly curved shallow shells by using an improved first-order shear deformation theory, Structures 64 (2024) 106594. https://doi.org/10.1016/j.istruc.2024.106594.

[9] J. Zhu, Z. Fang, X. Liu, J. Zhang, Y. Kiani, Vibration characteristics of skew sandwich plates with functionally graded metal foam core, Structures 55 (2023) 370–378. https://doi.org/10.1016/j.istruc.2023.06.039.

[10] T.A. Aslan, A.R. Noori, B. Temel, An efficient approach for free vibration analysis of functionally graded sandwich beams of variable cross-section, Structures 58 (2023) 105397. https://doi.org/10.1016/j.istruc.2023.105397.

[11] P. Phung-Van, C.H. Thai, T. Nguyen-Thoi, H. Nguyen-Xuan, Static and free vibration analyses of composite and sandwich plates by an edge-based smoothed discrete shear gap method (ES-DSG3) using triangular elements based on layerwise theory, Compos. Part. B-Eng. 60 (2014) 227–238. https://doi.org/10.1016/j.compositesb.2013.12.044.

[12] C.H. Thai, A.J.M. Ferreira, E. Carrera, H. Nguyen-Xuan, Isogeometric analysis of laminated composite and sandwich plates using a layerwise deformation theory, Compos. Struct. 104 (2013) 196–214. https://doi.org/10.1016/j.compstruct.2013.04.002.

[13] Bose P., Reddy J.N., Analysis of composite plates using various plate theories -Part 1:

Formulation and analytical solutions, Struct. Eng. Mech. 6 (1998) 583–612. https://doi.org/10.12989/SEM.1998.6.6.583.

[14] J.M. Whitney, N.J. Pagano, Shear Deformation in Heterogeneous Anisotropic Plates, J. Appl. Mech. 37 (1970) 1031–1036. https://doi.org/10.1115/1.3408654.

[15] J.N. Reddy, A Simple Higher-Order Theory for Laminated Composite Plates, J. Appl. Mech. 51 (1984) 745–752. https://doi.org/10.1115/1.3167719.

[16] B.N. Pandya, T. Kant, Higher-order shear deformable theories for flexure of sandwich plates—Finite element evaluations, Int. J. Solids Struct. 24 (1988) 1267–1286. https://doi.org/10.1016/0020-7683(88)90090-X.

[17] J.N. Reddy, A generalization of two-dimensional theories of laminated composite plates, Comm. App. Numer. Meth. 3 (1987) 173–180. https://doi.org/10.1002/cnm.1630030303.

[18] A.J.M. Ferreira, Analysis of Composite Plates Using a Layerwise Theory and Multiquadrics Discretization, Mech. Adv. Mat. Struct. 12 (2005) 99–112. https://doi.org/10.1080/15376490490493952.

[19] S.T. Mau, A Refined Laminated Plate Theory, J. Appl. Mech. 40 (1973) 606–607. https://doi.org/10.1115/1.3423032.

[20] M. Di Sciuva, An Improved Shear-Deformation Theory for Moderately Thick Multilayered Anisotropic Shells and Plates, J. Appl. Mech. 54 (1987) 589–596. https://doi.org/10.1115/1.3173074.

[21] A. Toledano, H. Murakami, A Composite Plate Theory for Arbitrary Laminate Configurations, J. Appl. Mech. 54 (1987) 181–189. https://doi.org/10.1115/1.3172955.

[22] C.H. Thai, A.J.M. Ferreira, M. Abdel Wahab, H. Nguyen-Xuan, A generalized layerwise higher-order shear deformation theory for laminated composite and sandwich plates based on isogeometric analysis, Acta Mech 227 (2016) 1225–1250. https://doi.org/10.1007/s00707-015-1547-4.

[23] H.-H. Phan-Dao, C.H. Thai, J. Lee, H. Nguyen-Xuan, Analysis of laminated composite and sandwich plate structures using generalized layerwise HSDT and improved meshfree radial point interpolation method, Aerosp. Sci. Technol. 58 (2016) 641–660. https://doi.org/10.1016/j.ast.2016.09.017.

[24] A.C. Eringen, Nonlocal polar elastic continua, Int. J. Eng. Sci. 10 (1972) 1–16. https://doi.org/10.1016/0020-7225(72)90070-5.

[25] R.D. Mindlin, Second gradient of strain and surface-tension in linear elasticity, Int. J. Solids Struct. 1 (1965) 417–438. https://doi.org/10.1016/0020-7683(65)90006-5.

[26] E.C. Aifantis, Strain gradient interpretation of size effects, in: Z.P. Bažant, Y.D.S. Rajapakse (Eds.), Fracture Scaling, Springer Netherlands, Dordrecht, 1999: pp. 299–314. https://doi.org/10.1007/978-94-011-4659-3_16.

[27] H.X. Nguyen, E. Atroshchenko, H. Nguyen-Xuan, T.P. Vo, Geometrically nonlinear isogeometric analysis of functionally graded microplates with the modified couple stress theory, Comput. Struct. 193 (2017) 110–127. https://doi.org/10.1016/j.compstruc.2017.07.017.

[28] S. Thai, H.-T. Thai, T.P. Vo, V.I. Patel, Size-dependant behaviour of functionally graded microplates based on the modified strain gradient elasticity theory and isogeometric analysis, Comput. Struct. 190 (2017) 219–241. https://doi.org/10.1016/j.compstruc.2017.05.014.

[29] B. Zhang, H. Li, L. Kong, J. Wang, H. Shen, Strain gradient differential quadrature beam finite elements, Comput. Struct. 218 (2019) 170–189.

https://doi.org/10.1016/j.compstruc.2019.01.008.

[30] P. Phung-Van, H. Nguyen-Xuan, P.T. Hung, C.H. Thai, Nonlinear isogeometric analysis of magneto-electro-elastic porous nanoplates, Appl. Math. Model. 128 (2024) 331–346. https://doi.org/10.1016/j.apm.2024.01.025.

[31] P. Phung-Van, L.B. Nguyen, P.T. Hung, H. Nguyen-Xuan, C.H. Thai, Nonlocal nonlinear analysis of functionally graded piezoelectric porous nanoplates, Int. J. Mech. Mater. Des. 20 (2024) 743–753. https://doi.org/10.1007/s10999-023-09701-5.

[32] N.-D. Nguyen, V.-T. Bui, T.-K. Nguyen, A modified strain gradient theory for buckling, bending and free vibration behaviors of metal foam microbeams, Structures 64 (2024) 106533. https://doi.org/10.1016/j.istruc.2024.106533.

[33] C.W. Lim, G. Zhang, J.N. Reddy, A higher-order nonlocal elasticity and strain gradient theory and its applications in wave propagation, J. Mech. Phy. Solids 78 (2015) 298–313. https://doi.org/10.1016/j.jmps.2015.02.001.

[34] C.H. Thai, A.J.M. Ferreira, P. Phung-Van, A nonlocal strain gradient isogeometric model for free vibration and bending analyses of functionally graded plates, Compos. Struct. 251 (2020) 112634. https://doi.org/10.1016/j.compstruct.2020.112634.

[35] C.H. Thai, P.T. Hung, H. Nguyen-Xuan, P. Phung-Van, A free vibration analysis of carbon nanotube reinforced magneto-electro-elastic nanoplates using nonlocal strain gradient theory, Finite Elem. Anal. Des. 236 (2024) 104154. https://doi.org/10.1016/j.finel.2024.104154.

[36] P. Phung-Van, A.J.M. Ferreira, H. Nguyen-Xuan, C.H. Thai, A nonlocal strain gradient isogeometric nonlinear analysis of nanoporous metal foam plates, Eng. Anal. Bound. Elem. 130 (2021) 58–68. https://doi.org/10.1016/j.enganabound.2021.05.009.

[37] C.H. Thai, A.J.M. Ferreira, H. Nguyen-Xuan, P. Phung-Van, A size dependent meshfree model for functionally graded plates based on the nonlocal strain gradient theory, Compos. Struct. 272 (2021) 114169. https://doi.org/10.1016/j.compstruct.2021.114169.

[38] P. Phung-Van, P.T. Hung, H. Nguyen-Xuan, C.H. Thai, Small scale analysis of porosity-dependent functionally graded triply periodic minimal surface nanoplates using nonlocal strain gradient theory, Appl. Math. Model. 127 (2024) 439–453. https://doi.org/10.1016/j.apm.2023.12.003.

[39] P. Phung-Van, P.T. Hung, C.H. Thai, Small-dependent nonlinear analysis of functionally graded triply periodic minimal surface nanoplates, Compos. Struct. 335 (2024) 117986. https://doi.org/10.1016/j.compstruct.2024.117986.

[40] P. Phung-Van, H. Nguyen-Xuan, P.T. Hung, M. Abdel-Wahab, C.H. Thai, Nonlocal strain gradient analysis of honeycomb sandwich nanoscale plates, Thin Wall. Struct.198 (2024) 111746. https://doi.org/10.1016/j.tws.2024.111746.

[41] P. Phung-Van, H. Nguyen-Xuan, C.H. Thai, Nonlocal strain gradient analysis of FG GPLRC nanoscale plates based on isogeometric approach, Eng. Comput. 39 (2023) 857–866. https://doi.org/10.1007/s00366-022-01689-4.

[42] C.H. Thai, P.T. Hung, H. Nguyen-Xuan, P. Phung-Van, A size-dependent meshfree approach for magneto-electro-elastic functionally graded nanoplates based on nonlocal strain gradient theory, Eng. Struct. 292 (2023) 116521. https://doi.org/10.1016/j.engstruct.2023.116521.

[43] C.H. Thai, A.M.J. Fereira, H. Nguyen-Xuan, P.T. Hung, P. Phung-Van, A nonlocal strain gradient isogeometric model for free vibration analysis of magneto-electro-elastic functionally graded nanoplates, Compos. Struct. 316 (2023) 117005.

https://doi.org/10.1016/j.compstruct.2023.117005.
[44] X. Zhang, Z. Zheng, L. Wang, H. Cui, X. Xie, H. Wu, X. Liu, B. Gao, H. Wang, P. Xiang, A quasi-distributed optic fiber sensing approach for interlayer performance analysis of ballastless track-type II plate, Opt. Laser Technol. 170 (2024) 110237. https://doi.org/10.1016/j.optlastec.2023.110237.
[45] X. Zhang, X. Xie, S. Tang, H. Zhao, X. Shi, L. Wang, H. Wu, P. Xiang, High-speed railway seismic response prediction using CNN-LSTM hybrid neural network, J. Civil Struct. Health. Monit. 14 (2024) 1125–1139. https://doi.org/10.1007/s13349-023-00758-6.
[46] A.A. Daikh, M.S.A. Houari, M.A. Eltaher, A novel nonlocal strain gradient Quasi-3D bending analysis of sigmoid functionally graded sandwich nanoplates, Compos. Struct. 262 (2021) 113347. https://doi.org/10.1016/j.compstruct.2020.113347.
[47] M. Sobhy, A comprehensive study on FGM nanoplates embedded in an elastic medium, Compos. Struct. 134 (2015) 966–980. https://doi.org/10.1016/j.compstruct.2015.08.102.
[48] C.H. Thai, A.J.M. Ferreira, H. Nguyen-Xuan, L.B. Nguyen, P. Phung-Van, A nonlocal strain gradient analysis of laminated composites and sandwich nanoplates using meshfree approach, Eng. Comput. 39 (2023) 5–21. https://doi.org/10.1007/s00366-021-01501-9.
[49] Q. Xia, P. Xiang, L. Jiang, J. Yan, L. Peng, Bending and free vibration and analysis of laminated plates on Winkler foundations based on meshless layerwise theory, Mech. Adv. Mater. Struc. 29 (2022) 6168–6187. https://doi.org/10.1080/15376494.2021.1972497.
[50] Z. Shao, Q. Xia, P. Xiang, H. Zhao, L. Jiang, Stochastic free vibration analysis of FG-CNTRC plates based on a new stochastic computational scheme, Appl. Math. Model. 127 (2024) 119–142. https://doi.org/10.1016/j.apm.2023.11.016.
[51] Q. Xia, P. Xiang, L. Peng, H. Wang, L. Jiang, Interlayer shearing and bending performances of ballastless track plates based on high-order shear deformation theory (HSDT) for laminated structures, Mech. Adv. Mater. Struc. (2023) 1–25. https://doi.org/10.1080/15376494.2022.2139441.
[52] Z. Shao, P. Xiang, H. Zhao, P. Zhang, X. Xie, L. Gan, W. Li, B. Yin, K.M. Liew, A novel train–bridge interaction computational framework based on a meshless box girder model, Adv. Eng. Softw. 192 (2024) 103628. https://doi.org/10.1016/j.advengsoft.2024.103628.
[53] Z. Shao, H. Zhao, P. Zhang, X. Xie, A.S. Ademiloye, P. Xiang, A meshless computational framework for a modified dynamic system of vehicle coupled with plate structure, Eng. Struct. 312 (2024) 118140. https://doi.org/10.1016/j.engstruct.2024.118140.
[54] P. Xiang, L. Zhang, K. Liew, A mesh-free computational framework for predicting vibration behaviors of microtubules in an elastic medium, Compos. Struct. 149 (2016) 41–53. https://doi.org/10.1016/j.compstruct.2016.03.063.
[55] J.S. Huang, J.X. Liew, A.S. Ademiloye, K.M. Liew, Artificial intelligence in materials modeling and design, Arch. Computat. Methods. Eng. 28 (2021) 3399–3413. https://doi.org/10.1007/s11831-020-09506-1.
[56] A.A. Daikh, I. Bensaid, A.M. Zenkour, Temperature dependent thermomechanical bending response of functionally graded sandwich plates, Eng. Res. Express 2 (2020) 015006. https://doi.org/10.1088/2631-8695/ab638c.
[57] C.H. Thai, A.J.M. Ferreira, H. Nguyen-Xuan, P. Phung-Van, A size dependent meshfree model for functionally graded plates based on the nonlocal strain gradient theory, Compos. Struct. 272 (2021) 114169. https://doi.org/10.1016/j.compstruct.2021.114169.

[58] J.N. Reddy, Mechanics of laminated composite plates and shells: theory and analysis, Second edition, CRC Press, Boca Raton London New York Washington, D.C, 2004.
[59] G.R. Liu, Y.T. Gu, A matrix triangularization algorithm for the polynomial point interpolation method, Comput. Method. Appl. M. 192 (2003) 2269–2295. https://doi.org/10.1016/S0045-7825(03)00266-4.
[60] X. Zhang, B. Chen, Z. Shao, Q. Wang, P. Xiang, A novel stochastic calculation scheme for dynamic response analysis of FG-GPLRC plate subject to a moving load, Acta Mech (2023). https://doi.org/10.1007/s00707-023-03813-x.
[61] B. Chen, Z. Shao, A.S. Ademiloye, D. Yang, X. Zhang, P. Xiang, Stochastic static analysis of functionally graded sandwich nanoplates based on a novel stochastic meshfree computational framework, Adv. Eng. Softw. 198 (2024) 103780. https://doi.org/10.1016/j.advengsoft.2024.103780.
[62] S. Srinivas, A refined analysis of composite laminates, J. Sound Vib. 30 (1973) 495–507. https://doi.org/10.1016/S0022-460X(73)80170-1.
[63] B.N. Pandya, T. Kant, Higher-order shear deformable theories for flexure of sandwich plates—Finite element evaluations, Int. J. Solids Struct. 24 (1988) 1267–1286. https://doi.org/10.1016/0020-7683(88)90090-X.
[64] A.J.M. Ferreira, C.M.C. Roque, P.A.L.S. Martins, Analysis of composite plates using higher-order shear deformation theory and a finite point formulation based on the multiquadric radial basis function method, Compos. Part. B-Eng. 34 (2003) 627–636. https://doi.org/10.1016/S1359-8368(03)00083-0.
[65] N. Grover, D.K. Maiti, B.N. Singh, A new inverse hyperbolic shear deformation theory for static and buckling analysis of laminated composite and sandwich plates, Comput. Struct. 95 (2013) 667–675. https://doi.org/10.1016/j.compstruct.2012.08.012.